J. Fluid Mech. (2007), *vol.* 577, *pp.* 211–239.
doi:10.1017/S0022112006004514 Printed in the United Kingdom

Modal and non-modal linear stability of the plane Bingham–Poiseuille flow

C. NOUAR[1], N. KABOUYA[1], J. DUSEK[2] AND M. MAMOU[3]

[1]LEMTA, UMR 7563 (CNRS-INPL-UHP), 2 Avenue de la Fort de Haye, BP 160 54504 Vandoeuvre Lès Nancy, France
cherif.nouar@ensem.inpl-nancy.fr

[2]IMFS Strasbourg, UMR 7507 (CNRS-ULP) 2 Rue Boussingault, 67000 Strasbourg, France

[3]Institute for Aerospace Research (IAR) National Research Council (NRC), Montreal Road, Ottawa, Ontario, Canada, K1A 0R6

(Received 2 March 2006 and in revised form 27 October 2006)

The receptivity problem of plane Bingham–Poiseuille flow with respect to weak perturbations is addressed. The relevance of this study is highlighted by the linear stability analysis results (spectra and pseudospectra). The first part of the present paper thus deals with the classical normal-mode approach in which the resulting eigenvalue problem is solved using the Chebychev collocation method. Within the range of parameters considered, the Poiseuille flow of Bingham fluid is found to be linearly stable. The second part investigates the most amplified perturbations using the non-modal approach. At a very low Bingham number ($B \ll 1$), the optimal disturbance consists of almost streamwise vortices, whereas at moderate or large B the optimal disturbance becomes oblique. The evolution of the obliqueness as function of B is determined. The linear analysis presented also indicates, as a first stage of a theoretical investigation, the principal challenges of a more complete nonlinear study.

1. Introduction

A viscoplastic fluid possesses a yield stress, τ_0, below which it either flows as an unsheared plug or does not flow. Bird, Dai & Yarusso (1983) gave a list of materials that fall into this category. According to these authors, the Bingham model is often used to describe the rheological behaviour of a viscoplastic fluid. For one-dimensional shear flow with a velocity $u(y)$ in the x-direction, the relationship between the shear stress τ_{xy} and the velocity gradient $\mathrm{d}u/\mathrm{d}y$, is given by

$$\left.\begin{array}{lll} \tau_{xy} = \mathrm{sgn}(\mathrm{d}u/\mathrm{d}y)\,\tau_0 + \mu_p \mathrm{d}u/\mathrm{d}y & \Leftrightarrow & |\tau_{xy}| > \tau_0 \\ \mathrm{d}u/\mathrm{d}y = 0 & \Leftrightarrow & |\tau_{xy}| \leqslant \tau_0, \end{array}\right\} \tag{1.1}$$

where sgn indicates the sign of the argument, μ_p is the plastic viscosity, and x and y are the streamwise and normal directions, respectively.

Shear flows of viscoplastic fluids are very common in oil wells, especially during drilling and cementing operations, and also in the food processing and in mining industries. For many of these applications, prediction of the flow regime can be of critical importance. Although commonly used as industrial fluids, there is surprisingly little published work that focuses on transition of these flows. Here, we consider the problem of transition in a yield-stress fluid flow in a plane channel geometry, which

is often used in an oilfield setting as an approximation of such flow in a narrow annulus.

Several phenomenological criteria for the transition have been proposed in the literature (Hedström 1952; Metzner & Reed 1955; Ryan & Johnson 1959; Hanks 1963; Hanks & Pratt 1967; Mishra & Tripathi 1971; Slatter 1999). The general approach consists of forming a parametric ratio of various physical flow quantities that are assumed to determine the stability of the flow. For Newtonian flows, the value of this parametric ratio at which the flow leaves the laminar regime is known or can be calculated. The same value is then assumed to be valid for a transition prediction in any purely viscous non-Newtonian fluid flow. However, when the rheological properties of the fluid depart significantly from the Newtonian case, the predictions provided by such phenomenological criteria diverge, and there is no way to determine which criterion is preferable.

To the best of our knowledge very few experimental studies on transition in Bingham (or Herschel–Bulkley) fluid flows are available in the literature. In all these experimental studies, the transition was partly triggered by intrinsic imperfections in the experimental setups. Hanks & Pratt (1967) reported experimental results which show that the transitional Reynolds number, R_T, increases significantly with the Bingham number B, defined as the ratio of the yield stress to a nominal viscous stress.

So far, no full theory of transition of channel flows exists, even for Newtonian fluids. Nevertheless significant progress has been achieved mainly due to the recognition of the relevance of the investigation of optimal disturbances. Evidence of transient growth preceding transition to turbulence has been found for example in numerical simulations by Henningson, Lundbladh & Johansson (1993) and in experimental studies by Klingmann (1992). An essential characteristic of the amplification of the perturbation energy is that it only applies to three-dimensional perturbations. For two-dimensional perturbations transient energy growth is far weaker than in the three-dimensional case (Farrell 1988; Butler & Farrell 1992). Work has been done in this direction for plane Poiseuille flow by Gustavsson (1991) and Reddy & Henningson 1993. The largest transient growths have been found for small streamwise wavenumbers.

To summarize, the works mentioned above state that a linear instability is not a necessary condition for triggering the transition of laminar flows. A strong non-normality of the linearized Navier–Stokes operator may be responsible for a significant amplification of disturbances, the spatial distribution and growth of which can be rigorously determined by the so-called non-modal analysis. This analysis remains, so far, basically linear. It is, however, believed that a sufficient growth of the original linear disturbances may trigger strongly nonlinear mechanisms capable of sustaining turbulence. This argument is much more than a pure mathematical speculation, as confirmed by the phenomenological formulae for pressure drop coefficients in ducts, where the wall roughness takes on, in a phenomenological manner, the role of the disturbances. In the absence of a fully nonlinear theory the non-modal analysis may provide a lower bound for the transition and indicates the disturbances most likely to be responsible for the transition.

The non-Newtonian Bingham case has not been investigated so far from this point of view. Frigaard, Howison & Sobey (1994) performed a linear stability analysis, with a modal approach, of plane Poiseuille flow of a Bingham fluid subjected to two-dimensional disturbances. To be consistent with Newtonian fluid results, the eigenvalue problem obtained (linear stability equations)-was solved with modified boundary conditions at the yield surface. One can note that from the experimental

point of view a more accurate characterization of viscoplastic behaviour may necessitate more complex models (such as the Herschel–Bulkley one); however the most important features of viscoplastic fluid flows – the presence of a plug zone and yield surfaces as well as the shear-thinning behaviour of the effective viscosity – are rendered well by the simple Bingham model. Therefore the theoretical studies retain this model as a reference for the fundamental theoretical development.

For Bingham fluids and other nonlinear viscous fluids, there is no equivalent of Squire's theorem, unless unphysical restrictions are imposed (Georgievskii 1993). Then, three-dimensional disturbances must be considered. Using essentially Singe's method (Synge 1938), Frigaard & Nouar (2003) derived the eigenvalue bounds of the three-dimensional linear stability problem. They showed that for large Bingham numbers, the upper bound for the Reynolds number at which three-dimensional linear stability can be achieved has the form of $Re = O(B^{3/4})$ for all wavelengths. A nonlinear stability analysis based on the energy method was performed by Nouar & Frigaard (2001). The critical Reynolds number, Re_E, below which the kinetic energy of any finite-amplitude disturbance decays monotonically in time was determined. For large B, the authors found that $Re_E = O(B^{1/2})$. There was no direct contribution of the yield stress to the viscous dissipation in their analysis. The effect of τ_0 on Re_E arose only from the modification of the width of the yielded zone and via the velocity gradient of the base flow. These relevant theoretical studies lead to analytical expressions for the dependence of the critical conditions on the Bingham number. However, they provide insufficient insight into the instability mechanism. Moreover, the bounds obtained are not sharp because they were derived using functional inequalities rather than computed values.

Poiseuille flow of Bingham fluid, referred to hereafter as plane Bingham–Poiseuille flow (PBPF), is characterized particularly by the existence of a plug zone moving as a rigid body and a yielded zone in which the effective viscosity varies with the second invariant of the rate of strain tensor. This particular flow pattern may modify the transient growth compared to a Newtonian flow. The aim of the present investigation is to determine the influence of B on the transient growth and on the optimal perturbation, i.e. the initial conditions that provide the maximal energy growth. Trefethen *et al.* (1993) showed that the transient growth is closely associated with the sensitivity of the spectrum to small perturbations of the stability operator, quantified by the pseudospectra. Therefore, it is first necessary to revisit the classical linear stability problem using a modal approach with the exact boundary conditions at the yield surface, in order to determine the properties of the eigenvalue spectra in two- and three-dimensional situations. To the best of our knowledge, this has not been done previously. Moreover, the three-dimensional situation has not yet been considered despite the fact that there is no equivalent to Squire's theorem for Bingham fluids flows.

The paper is organized as follows. Section 2 recalls the characteristics of plane Bingham–Poiseuille flow. The equations governing the linear stability problem are derived in § 3. A scalar product and its associated norm based on energy density are introduced, and the techniques used to characterize the transient growth are developed. In § 4, the numerical method used to solve the eigenvalue problem is presented. Section 5 is dedicated to an analysis and discussion of the results. It is divided into three parts: § 5.1 is devoted to spectra properties, § 5.2 is concerned with describing the pseudospectra and § 5.3 deals with the transient growth and optimal perturbation. Conditions for no energy growth are derived in § 6, and some concluding remarks on the findings are itemized in § 7.

2. Equations of motion: plane Bingham–Poiseuille flow

A plane channel flow of an incompressible Bingham fluid with a yield stress τ_0 and a plastic viscosity μ_p is considered. The governing equations written in dimensionless form are

$$\nabla \cdot \boldsymbol{U} = 0, \tag{2.1}$$

$$\frac{\partial \boldsymbol{U}}{\partial t} + (\boldsymbol{U} \cdot \nabla)\boldsymbol{U} = -\nabla p + \nabla \cdot \boldsymbol{\tau}(\boldsymbol{U}), \tag{2.2}$$

where $\boldsymbol{U}$ is the velocity, p is the pressure and $\boldsymbol{\tau}$ is the deviatoric extra-stress tensor. The velocity vector is of the form $\boldsymbol{U} = U\boldsymbol{e}_x + V\boldsymbol{e}_y + W\boldsymbol{e}_z$, where U, V, W are the velocity components, and $\boldsymbol{e}_x$, $\boldsymbol{e}_y$, $\boldsymbol{e}_z$ are unit vectors in the streamwise (x), normal to wall (y), and spanwise (z) directions, respectively. The above equations are non-dimensionalized using the half-width of the channel H as the length scale, the maximum velocity U_0 of the base flow as the velocity scale and the dynamic pressure $\rho {U_0}^2$ as the stress and pressure scale.

Using the Von Mises yield criterion for the flow, Oldroyd (1947*a*, *b*) formulated the constitutive relations between stress, strain and strain rate for a Bingham fluid by assuming an elastic response prior to yielding and a viscous response afterwards. The elastic behaviour is generally neglected (Beris *et al.* 1985; (1947*a*, *b*) Coussot 1999) and the constitutive equations can be written after scaling as

$$\boldsymbol{\tau} = \mu \dot{\boldsymbol{\gamma}} \Leftrightarrow \tau > \frac{B}{Re}, \tag{2.3}$$

$$\dot{\gamma} = 0 \Leftrightarrow \tau \leqslant \frac{B}{Re}, \tag{2.4}$$

with

$$\mu = \frac{1}{Re}\left(1 + \frac{B}{\dot{\gamma}}\right), \tag{2.5}$$

where $\dot{\gamma} = \sqrt{\dot{\gamma}_{ij}\dot{\gamma}_{ij}/2}$ and $\tau = \sqrt{\tau_{ij}\tau_{ij}/2}$ are the second invariants of the strain rate $\dot{\boldsymbol{\gamma}}$ and deviatoric stress tensors $\boldsymbol{\tau}$ respectively and μ is a dimensionless effective viscosity. The components of $\dot{\boldsymbol{\gamma}}$ are $\dot{\gamma}_{ij} = U_{i,j} + U_{j,i}$. The dimensionless parameters B and Re are respectively the Bingham and Reynolds numbers

$$B = \frac{\tau_0 H}{\mu_p U_0}, \quad Re = \frac{\rho U_0 H}{\mu_p}. \tag{2.6}$$

In the regions where the yield stress is not exceeded, the rate of strain tensor is identically zero and the stress tensor is undetermined. The fluid within these regions is constrained to move as a rigid body. These regions are called unyielded or plug zones. The interface between the yielded and the unyielded zones is called the yield surface. Its location is determined via the yield criterion, which is given in dimensionless form as $\tau = B/Re$. The stress, $-p\delta_{ij} + \tau_{ij}$, and the velocity components are continuous across the yield surface.

For one-dimensional shear flow, the pressure P_b and the axial velocity profile $U_b(y)$ are given by

$$P_b = -\frac{2B}{Re(1 - y_0)^2}x + \text{constant}, \tag{2.7}$$

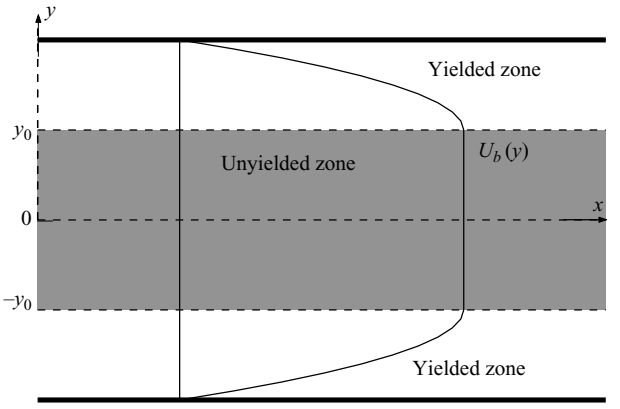

FIGURE 1. Plane Bingham–Poiseuille flow configuration.

$$U_b(y) = \begin{cases} 1, & 0 \leqslant |y| < y_0, \\ 1 - \left(\dfrac{|y| - y_0}{1 - y_0}\right)^2, & y_0 \leqslant |y| \leqslant 1. \end{cases} \tag{2.8}$$

An example of velocity profile is illustrated in figure 1. At the yield surfaces ($y = \pm y_0$), we have $|\tau_{xy}| = B/Re$. Using the relation $|\tau_w| = B/(Rey_0)$, where $|\tau_w|$ is the wall shear stress, the position y_0 of the yield surface is the solution to the equation

$$B(1 - y_0)^2 - 2y_0 = 0, \tag{2.9}$$

which is given by

$$y_0 = \frac{1}{B}(B + 1 - \sqrt{2B + 1}). \tag{2.10}$$

3. Linear stability analysis

3.1. *Perturbation equations*

Following the usual linear stability analysis, an infinitesimal perturbation $(\epsilon \boldsymbol{u}', \epsilon p')$ with $\epsilon \ll 1$ is imposed on the base flow $(\boldsymbol{U}_b, P_b)$. The perturbed flow is given by

$$(\boldsymbol{U}_b + \epsilon \boldsymbol{u}', P_b + \epsilon p') = (U_b + \epsilon u', \epsilon v', \epsilon w', P_b + \epsilon p'). \tag{3.1}$$

Wherever the yield stress is exceeded, the effective viscosity of the perturbed flow is expanded about the base flow:

$$\mu(\boldsymbol{U}_b + \epsilon \boldsymbol{u}') = \mu(\boldsymbol{U}_b) + \epsilon \dot{\gamma}_{ij}(\boldsymbol{u}') \frac{\partial \mu}{\partial \dot{\gamma}_{ij}}(\boldsymbol{U}_b) + O(\epsilon^2). \tag{3.2}$$

Using (2.3), (2.5) and (3.2), the components τ_{ij} of the deviatoric stress tensor for the disturbed flow can be expressed as

$$\tau_{ij}(\boldsymbol{U}_b + \epsilon \boldsymbol{u}') = \tau_{ij}(\boldsymbol{U}_b) + \epsilon \tau'_{ij} + O(\epsilon^2), \tag{3.3}$$

with

$$\tau'_{ij} = \mu(\boldsymbol{U}_b)\dot{\gamma}_{ij}(\boldsymbol{u}') = \frac{1}{Re}\left(1 + \frac{B}{|\mathrm{D}U_b|}\right)\dot{\gamma}_{ij}(\boldsymbol{u}') \quad \text{if} \quad ij \neq xy, yx, \tag{3.4}$$

$$\tau'_{ij} = \frac{1}{Re}\dot{\gamma}_{ij}(\boldsymbol{u}') \quad \text{if} \quad ij = xy, yx, \tag{3.5}$$

where $\mathrm{D} \equiv \mathrm{d}/\mathrm{d}y$. It is interesting to observe that τ'_{xy} is independent of B. Then, the perturbation shear stress tensor τ'_{ij} is anisotropic. This is a consequence of non-constant $\mu(\boldsymbol{U}_b)$. The effects on the additional viscous dissipation due to the Bingham terms will be also anisotropic.

From (3.3), it follows that the second invariant of the deviatoric of the stress tensor is linearly perturbed: $|\tau(\boldsymbol{U}_b + \epsilon\boldsymbol{u}') - \tau(\boldsymbol{U}_b)| = O(\epsilon)$. Therefore, it can be assumed that the yield surface positions $y_Y^{\pm}$ will be also linearly perturbed from their initial position $\pm y_0$:

$$y_Y^{\pm}(\boldsymbol{U}_b + \epsilon\boldsymbol{u}') = \pm\, y_0 \pm \epsilon h^{\pm}(x, z, t). \tag{3.6}$$

The linearized perturbation equations in the two yielded zones have been derived by Frigaard *et al.* (1994) and Frigaard & Nouar (2003), in a standard way. These authors showed that the linear stability problems in the two yielded regions decouple and are equivalent; therefore, only one domain is considered, say $y \in [y_0, 1]$. The disturbance quantities $\boldsymbol{u}'$, p' and $h^{\pm}$ are assumed periodic and of the form

$$(u', v', w', p', h^{\pm}) = (u(y,t), v(y,t), w(y,t), p(y,t), h^{\pm}(t))\mathrm{e}^{\mathrm{i}(\alpha x + \beta z)}, \tag{3.7}$$

where α and β are taken to be real and are the wavenumbers in the x- and z-directions, respectively. Using (3.7) and assuming that $\alpha \neq 0$ or $\beta \neq 0$, the following initial value problem is obtained:

$$\mathrm{i}[\alpha u + \beta w] + \mathrm{D}v = 0, \tag{3.8}$$

$$\frac{\partial u}{\partial t} = -\mathrm{i}\alpha U_b u - v\mathrm{D}U_b - \mathrm{i}\alpha p + \frac{1}{Re}\mathscr{F}u + \frac{B}{Re}\left[\frac{-k^2 u - \mathrm{i}\alpha \mathrm{D}v}{|\mathrm{D}U_b|}\right], \tag{3.9}$$

$$\frac{\partial v}{\partial t} = -\mathrm{i}\alpha U_b v - \mathrm{D}p + \frac{1}{Re}\mathscr{F}v + \frac{B}{Re}\left[\mathrm{D}\left(\frac{2\mathrm{D}v}{|\mathrm{D}U_b|}\right) + \frac{-\beta^2 v + \mathrm{i}\beta \mathrm{D}w}{|\mathrm{D}U_b|}\right], \tag{3.10}$$

$$\frac{\partial w}{\partial t} = -\mathrm{i}\alpha U_b w - \mathrm{i}\beta p + \frac{1}{Re}\mathscr{F}w + \frac{B}{Re}\left[\mathrm{D}\left(\frac{\mathrm{i}\beta v + \mathrm{D}w}{|\mathrm{D}U_b|}\right) - \frac{k^2 w + \mathrm{i}\beta \mathrm{D}v}{|\mathrm{D}U_b|}\right], \tag{3.11}$$

with $\mathscr{F} \equiv \mathrm{D}^2 - k^2$ and $k^2 = \alpha^2 + \beta^2$. The boundary conditions at the wall, $y = 1$, and at the yield surface $y = y_0$, are

$$u(1) = v(1) = w(1) = 0, \tag{3.12}$$

$$u(y_0) = v(y_0) = w(y_0) = 0, \tag{3.13}$$

$$\mathrm{D}v(y_0) = \mathrm{D}w(y_0) = 0,\ \mathrm{D}u(y_0) = -h\mathrm{D}^2 U_b(y_0). \tag{3.14}$$

The Dirichlet boundary conditions $\boldsymbol{u}' = 0$ at the yield surface come from the fact that the unyielded plug zone is constrained to move as a rigid body according to the Bingham model (2.4). As with any rigid body motion, the velocity within the plug can be decomposed instantaneously into a linear motion and a rotation about an instantaneous centre of mass of the plug zone. As the perturbation is periodic, the plug zone can only have a linear motion. As a consequence, inside the plug, $U_b + \epsilon u'$, v' and w' are independent of the spatial coordinates. With the help of velocity continuity across the yield surface, it follows that the fluid particles at the yield surface satisfy $(\partial/\partial x)(\boldsymbol{U}_b + \epsilon\boldsymbol{u}') = (\partial/\partial z)(\boldsymbol{U}_b + \epsilon\boldsymbol{u}') = 0$ at $y = y_Y^{\pm}$. Combining this condition with (3.7) lead at the first order to $\boldsymbol{u}' = 0$ at $\pm y_0$. The interpretation of the other boundary conditions at $\pm y_0$ is given by Frigaard & Nouar (2003).

The system of equations (3.8)–(3.11) can be expressed in terms of u and v if $\beta \neq 0$ or v and w if $\alpha \neq 0$, or in terms of v and the y-component of the vorticity,

$\eta = \mathrm{i}\beta u - \mathrm{i}\alpha w$. For this last formulation, unlike Newtonian fluids, the Bingham terms do not allow us to obtain an Orr–Sommerfeld-like equation for v decoupled from the η-equation. The results presented in this paper were obtained using the (u, v) or (v, w) formulation, and some of them were checked with the (u, v, w, p) formulation.

3.2. *Long-time behaviour of the disturbance: eigenvalue problem*

Assuming solutions of the form $\boldsymbol{\psi} = \hat{\boldsymbol{\psi}} \exp(-\mathrm{i}\omega t)$, where the vector $\boldsymbol{\psi}$ stands for $(u, v)^T$ or $(v, w)^T$, depending on whether the (u, v) or (v, w) formulation is used, the corresponding initial-value problem is transformed into a generalized eigenvalue problem with the complex frequency ω as the eigenvalue. It can be formally written as

$$\mathscr{L}_{vw}(\hat{v}, \hat{w})^T = \omega \mathscr{M}_{vw}(\hat{v}, \hat{w})^T, \tag{3.15}$$

or

$$\mathscr{L}_{uv}(\hat{u}, \hat{v})^T = \omega \mathscr{M}_{uv}(\hat{u}, \hat{v})^T. \tag{3.16}$$

The growth (or decay) rate of the amplitude of a given mode is determined by the sign of $\omega_i = \mathrm{Im}(\omega)$: the amplitude will grow exponentially in time if $\omega_i > 0$ and will decay exponentially in time if $\omega_i < 0$. The real part ω_r is the circular frequency and the ratio ω_r/α is the phase velocity.

3.3. *Transient growth and optimal disturbance*

The transient evolution of a perturbation in the linear regime is determined by following the methodology described by Schmid & Henningson (1994). It is presented here only for the (u, v) formulation, but a similar development applies to the (v, w) or other formulations. We introduce a velocity disturbance vector-function $\boldsymbol{q} = (u, v)^T$ and a scalar product based on the energy density,

$$(\boldsymbol{q}_1, \boldsymbol{q}_2)_E = \int_{y_0}^{1} \left[\frac{k^2}{\beta^2} u_1^* u_2 + v_1^* v_2 + \frac{1}{\beta^2} \mathrm{D}v_1^* \mathrm{D}v_2 + \frac{\mathrm{i}\alpha}{\beta^2} (\mathrm{D}v_1^* u_2 - u_1^* \mathrm{D}v_2) \right] \mathrm{d}y, \tag{3.17}$$

where $*$ denotes the complex conjugate. Therefore, the associated norm is given as

$$\|\boldsymbol{q}\|_E^2 = (\boldsymbol{q}, \boldsymbol{q})_E. \tag{3.18}$$

Let us consider the linear subspace S_M spanned by the M eigenfunctions $\hat{\boldsymbol{q}}_j = (\hat{u}_j, \hat{v}_j)^T$ corresponding to the first M eigenvalues $\{\omega_1, \omega_2, \ldots, \omega_M\}$ of the spectrum of $\mathscr{A}_{uv} = \mathscr{M}_{uv}^{-1} \mathscr{L}_{uv}$ sorted in decreasing order of their imaginary parts:

$$\mathscr{S}_M = \mathrm{span}\{\hat{\boldsymbol{q}}_1, \hat{\boldsymbol{q}}_2, \ldots, \hat{\boldsymbol{q}}_M\}.$$

An admissible perturbation $\boldsymbol{q}$ is expressed as a linear combination of the eigenfunctions $\hat{\boldsymbol{q}}_j$,

$$\boldsymbol{q} = \sum_{j=1}^{M} \kappa_j \hat{\boldsymbol{q}}_j, \tag{3.19}$$

Its energy growth is measured by the ratio $g(t)$ between the energy norm $\|\boldsymbol{q}(t)\|_E^2$ of the perturbation at time t and its initial norm $\|\boldsymbol{q}_0\|_E^2$:

$$g(t) = \frac{\|\boldsymbol{q}(t)\|_E^2}{\|\boldsymbol{q}_0\|_E^2}. \tag{3.20}$$

For a given set of values of α, β, Re, and B, the maximum possible energy amplification at time t over all possible initial combinations of the M eigenfunctions, is denoted by

$$G(t) = \sup_{\|\boldsymbol{q}_0\|_E^2 \neq 0} g(t). \tag{3.21}$$

The maximum growth for all time t is denoted by

$$G^{max}(\alpha, \beta, Re, B) = G^{max} = \sup_{t \geqslant 0} G(t). \tag{3.22}$$

The quantity G^{max} is associated with a particular initial disturbance that reaches G^{max} at a specific time $t^{max}(\alpha, \beta, Re, B)$, i.e. $G^{max} = G(t^{max})$.

The maximum of G^{max} for all the pairs $(\alpha, \beta) \in R^+ \times R^+$ is denoted $G^{opt}(Re, B) = \sup_{\alpha,\beta} G^{max}(\alpha, \beta, Re, B)$ and corresponds to the optimal perturbation. Finally, one can define a specific time $t^{opt}(Re, B)$ related to $G^{opt}(Re, B)$.

4. Numerical method

As the width $(1-y_0)$ of the yielded zone varies with B, it is useful to map the domain $y \in [y_0, 1]$ onto $\tilde{y} \in [0, 1]$ by substituting $y = \tilde{y}(1 - y_0) + y_0$. This leads to the scaling $\phi = \tilde{\phi}(1-y_0)$ for the problem variables such as $\phi \equiv x, z, t$ and the scaling $\tilde{\zeta} = \zeta(1-y_0)$ for the problem parameters $\zeta \equiv \alpha, \beta, \omega, Re, B$. With the introduction of the scaled variables and parameters denoted by the tilde, the expressions for the initial-value problems and the eigenvalue problems remain unchanged. In terms of $\tilde{y}$, the basic flow velocity profile $U_b = 1 - \tilde{y}^2$ is artificially independent of the Bingham number.

A spectral collocation method based on Chebychev polynomials is applied to compute the eigenvalues and the corresponding eigenfunctions of the system (3.15) or (3.16). The equations are discretized on the Gauss–Lobato grid. The generalized eigenvalue matrix system obtained is solved using the QZ algorithm available in the Matlab-software package. The details of the procedure are reported by Schmid & Henningson (2000). Calculations are performed for $\widetilde{Re} \leqslant 3 \times 10^4$, $0.02 \leqslant \tilde{B} \leqslant 40$, $\tilde{\alpha} \leqslant 5$ and $\tilde{\beta} \leqslant 5$. Spectra with increasing collocation points ($N = 32, 64, 96, 128 \ldots$) were compared to determine the adequate number $(N+1)$ of Chebychev polynomials. It is found that with $N = 128$, the first 40 eigenvalues taken in order of increasing absolute value of their imaginary part were resolved accurately within five digits (i.e. invariant digits when N is increased) for almost all the situations considered in this paper. For Newtonian plane Poiseuille flow, our results with a truncation $N = 64$ to 5 significant digits agree with the results reported by Orszag (1971).

The computation of the eigenmodes can be performed using the (u, v, w, p) formulation as described by Khorrami, Malik & Ash (1989). This formulation remains valid even if $\alpha = 0$ or $\beta = 0$. However, the size of the matrices is increased to $4(N+1) \times 4(N+1)$, while for the (u, v) or (v, w) formulations, the matrices are only $2(N+1) \times 2(N+1)$. Therefore, more computational time is required for the (u, v, w, p) formulation. Nevertheless, several tests are performed to ensure that the three formulations lead to the same results.

5. Results

The aim of the present study is to understand the influence of the Bingham number on the flow stability. This influence arises from five different effects: (i) variation of the inertial terms, (ii) variation of the width of the plug zone, (iii) boundary conditions

for the perturbation at the yield surface, (iv) shear-thinning behaviour of the effective viscosity which leads here to an anisotropy of the perturbation shear stress tensor, and (v) variation of the dissipative terms. It is clear that it is of interest to understand the contributions of these individual effects. The scaling parameters used in § 2 and the introduction of the tilde variables in the § 4, allow us to implicitly account for the modification of the plug zone width and of the shear rate when B varies. If the Bingham terms in the system (3.8)–(3.14) written with a tilde are cancelled artificially, we recover the linear stability problem of the Couette–Poiseuille flow of a Newtonian fluid, where the upper plate ($\tilde{y}=1$) is fixed and the lower plate ($\tilde{y}=0$) is moving with a constant velocity $U_c=1$. The velocity profile, $U_b=1-\tilde{y}^2$, can be written as the sum of Couette ($1-\tilde{y}$) and Poiseuille ($U_p=\tilde{y}-\tilde{y}^2$) components. This plane Newtonian Couette–Poiseuille flow (PNCPF) permits the effect of the vanishing of the perturbation at the yield surface to be separated out.

5.1. *Long-time behaviour of the disturbance*

Depending on the wavenumbers $\tilde{\alpha}$ and $\tilde{\beta}$, four types of disturbances can be considered: (i) one-dimensional perturbation ($\tilde{\alpha}=\tilde{\beta}=0$), (ii) streamwise perturbation ($\tilde{\alpha}\neq 0, \tilde{\beta}=0$), (iii) spanwise perturbation ($\tilde{\alpha}=0, \tilde{\beta}\neq 0$) and (iv) oblique perturbation $\tilde{\alpha}\neq 0, \tilde{\beta}\neq 0$. The one-dimensional analysis ($\tilde{\alpha}=\tilde{\beta}=0$) was performed by Frigaard *et al.* (1994), who demonstrated that this mode is unconditionally linearly stable. In the present study, some new results are presented and discussed for the three remaining situations.

5.1.1. *Streamwise perturbation: $\beta=0$*

The (v, w) formulation was considered for the two-dimensional streamwise perturbation. The linear stability equations reduce to two decoupled differential equations: (i) a fourth-order differential equation for $\hat{v}$, which is similar to the Orr–Sommerfeld equation with an additional Bingham term and (ii) a second-order differential equation for $\hat{w}$, which is similar to the Squire equation with an additional Bingham term. These will be referred to as the Bingham–Orr–Sommerfeld and Bingham–Squire equations respectively. In the following discussion, the characteristics of the Bingham–Orr–Sommerfeld modes and Bingham–Squire modes are described in detail. The Bingham–Orr–Sommerfeld spectra obtained for $\tilde{\alpha}=1, \widetilde{Re}=10^4$ and different values of $\tilde{B}$ are illustrated in figure 2. The eigenvalues (particularly the A-family) are weakly sensitive to an increase of $\tilde{B}$. To interpret this result, the Bingham–Orr–Sommerfeld equation is multiplied by the complex conjugate v^* and integrated between the yield surface ($\tilde{y}=0$) and the wall ($\tilde{y}=1$). In the following, the hat on u, v and w is dropped for simplicity. Hence, we obtain

$$\tilde{\omega}_i\langle|\tilde{\mathrm{D}}v|^2+\tilde{\alpha}^2|v|^2\rangle=\tilde{\alpha}\langle(v_r\tilde{\mathrm{D}}v_i-v_i\tilde{\mathrm{D}}v_r)\tilde{\mathrm{D}}U_b\rangle \\ -\frac{1}{\widetilde{Re}}\langle|\tilde{\mathrm{D}}^2v|^2+\tilde{\alpha}^4|v|^2+2\tilde{\alpha}^2|\tilde{\mathrm{D}}v|^2\rangle-4\tilde{\alpha}^2\frac{\tilde{B}}{\widetilde{Re}}\left\langle\frac{|\tilde{\mathrm{D}}v|^2}{|\tilde{\mathrm{D}}U_b|}\right\rangle \quad (5.1)$$

and

$$\tilde{\omega}_r\langle|\tilde{\mathrm{D}}v|^2+\tilde{\alpha}^2|v|^2\rangle=\tilde{\alpha}\langle\tilde{\mathrm{D}}^2U_b|v|^2+U_b(\tilde{\alpha}^2|v|^2)+|\tilde{\mathrm{D}}v|^2)\rangle \\ +\tilde{\alpha}\langle(\tilde{\mathrm{D}}v_rv_r+\tilde{\mathrm{D}}v_iv_i)\tilde{\mathrm{D}}U_b\rangle, \quad (5.2)$$

where $|v|^2=v_r^2+v_i^2$ and $\langle.\rangle=\displaystyle\int_0^1(.)\,\mathrm{d}\tilde{y}$.

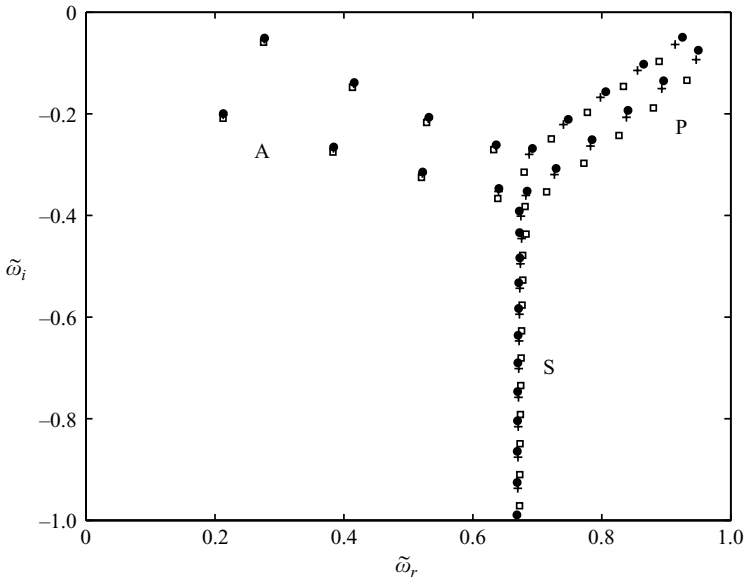

FIGURE 2. Bingham–Orr–Sommerfeld spectra for $\tilde{\alpha} = 1$ and $\widetilde{Re} = 10^4$. ●, $\tilde{B} = 0.02$, $y_0 \approx 0.01$; +, $\tilde{B} = 10$, $y_0 \approx 0.83$ □; $\tilde{B} = 40$, $y_0 \approx 0.95$. The constituents of the spectra are classified into three groups labelled A, P, and S families as suggested by Mack (1976): (i) family A exhibit a low phase velocity and correspond to the wall modes; (ii) family P with a phase velocity $\omega_r/\alpha \approx 1$ correspond to the modes concentrated near the yield surface and (iii) family S correspond to the mean modes with phase velocity $\omega_r/\alpha \approx 2/3$.

One can observe that: (i) there is no Bingham term in the expression for $\tilde{\omega}_r$; (ii) the Bingham number plays the role of a dissipation term in (5.1); and (iii) the viscous dissipation originating from the plastic viscosity contains a term of a second-order derivative of v, $-(1/\widetilde{Re})\langle|\tilde{\mathrm{D}}^2 v|^2\rangle$, while the viscous dissipation due to the Bingham number involves only a first-order derivative of v. This is a consequence of the fact that τ'_{xy} does not depend on B, as indicated in § 3.1. The profiles of the different terms of (5.1) shows, in particular for the wall modes, that $\langle|\tilde{\mathrm{D}}v|^2/|\tilde{\mathrm{D}}U_b|\rangle < 0.01\ \langle|\tilde{\mathrm{D}}^2 v|^2\rangle$. Therefore, if $\tilde{\alpha}$ and $\tilde{B}$ do not exceed $O(1)$, the viscous dissipation due to the Bingham term remains much lower than the pure viscous dissipation (originating from the plastic viscosity). A rough analysis can be made to estimate a magnitude order of $\tilde{B}$ below which the viscous dissipation due to the Bingham number can be neglected in comparison with the pure viscous dissipation. Using Poincaré inequality and assuming $|\tilde{\mathrm{D}}U_b| \approx 1$, since the eigenfunction for the wall modes is large, particularly near the wall, $\tilde{B} \leqslant O(\pi^2/4\tilde{\alpha}^2 + 0.5)$.

For the P-modes, the eigenfunctions are localized near the yield surface where the shear rate tends to zero. The viscous dissipation due to the Bingham terms increases significantly, inducing a decrease of $\tilde{\omega}_i$.

For $\tilde{\alpha} \neq 1$, the shape of the Bingham–Orr–Sommerfeld spectrum is similar to that of $\tilde{\alpha} = 1$ if it is represented in terms of $(\omega_i/\alpha, \omega_r/\alpha)$. The variation of the eigenmodes as $\tilde{\alpha}$ changes is shown in figure 3(a, b), where ω_i/α and ω_r/α of the four least stable eigenmodes are plotted as function of $\tilde{\alpha}$ for $\tilde{\alpha}\widetilde{Re} = 5000$, $\tilde{\beta} = 0$ and $\tilde{\alpha}^2\tilde{B} = 2$.

Concerning the Bingham–Squire modes, it can be shown that

$$\tilde{\omega}_i\langle|w|^2\rangle = -\frac{1}{\widetilde{Re}}\left\langle\left(1 + \frac{\tilde{B}}{|\tilde{\mathrm{D}}U_b|}\right)(|\tilde{\mathrm{D}}w|^2 + \tilde{k}^2|w|^2)\right\rangle < 0, \tag{5.3}$$

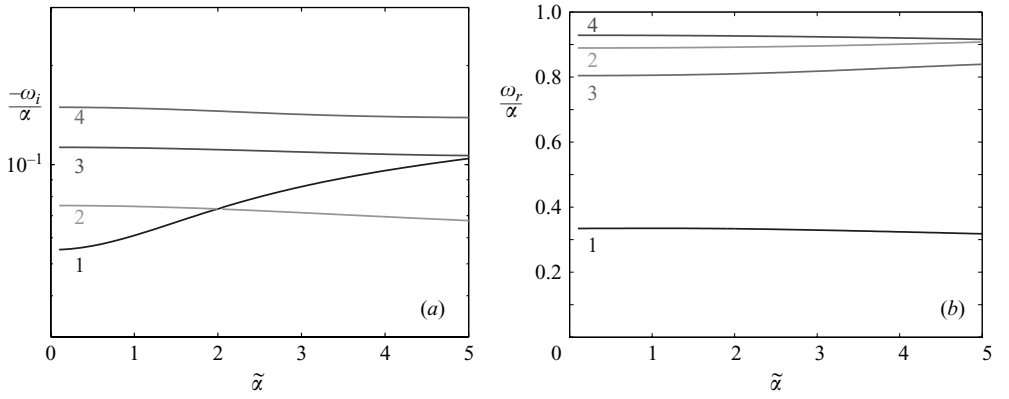

FIGURE 3. Variation of (*a*) $-\omega_i/\alpha$ and (*b*) ω_r/α for the first four eigenvalues with streamwise wavenumber $\tilde{\alpha}$, at $\tilde{\alpha}\widetilde{Re} = 5000$ and $\tilde{\alpha}^2\tilde{B} = 2$.

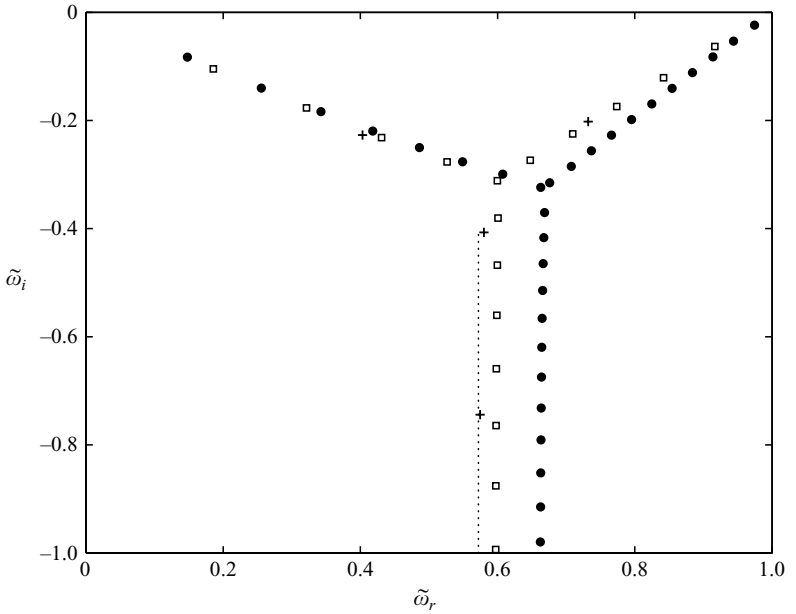

FIGURE 4. Bingham–Squire spectra for $\tilde{\alpha} = 1$, $\widetilde{Re} = 10^4$ and three values of $\tilde{B}$. The solid circles correspond to $\tilde{B} = 0.02$, the squares to $\tilde{B} = 2$ and the pluses to $\tilde{B} = 40$. The dotted line is the phase velocity of the spectrum stem when the viscous dissipation in the Bingham–Squire equation is assumed due only to the Bingham terms.

and

$$\tilde{\omega}_r \langle |w|^2 \rangle = \tilde{\alpha} \langle U_b |w|^2 \rangle. \tag{5.4}$$

The Bingham–Squire modes are thus always damped and the Bingham number has a stabilizing effect. Figure 4 shows the Bingham–Squire family for $\tilde{\alpha} = 1$, $\widetilde{Re} = 10^4$ and three values of $\tilde{B}$: 0.02, 2 and 40. As expected, a significant decrease of $\tilde{\omega}_i$ is observed as $\tilde{B}$ increases. We also note, a decrease of the stem phase velocity, $\tilde{\omega}_r/\tilde{\alpha}_r$, with increasing $\tilde{B}$. The numerical results show that for given $\widetilde{Re}$, and increasing

$\tilde{B}$, the stem phase velocity decreases from $c_r \approx 2/3$ and tends towards an asymptotic value of 0.572. This asymptotic value is the stem phase velocity of the eigenvalue spectrum when the viscous dissipation in the Bingham–Squire equation is assumed to be due only to the Bingham terms.

5.1.2. *Spanwise perturbation:* $\alpha = 0$

On setting $\alpha = 0$, the linear stability equations given by the (u, v) formulation reduce to

$$(\tilde{\mathrm{D}}^2 - \tilde{\beta}^2)u - \widetilde{Re}\tilde{\mathrm{D}}U_b v = -\mathrm{i}\widetilde{Re}\tilde{\omega}u + \frac{\tilde{B}}{|\tilde{\mathrm{D}}U_b|}\tilde{\beta}^2 u, \tag{5.5}$$

$$(\tilde{\mathrm{D}}^2 - \tilde{\beta}^2)^2 v = -\mathrm{i}\tilde{\omega}\widetilde{Re}(\tilde{\mathrm{D}}^2 - \tilde{\beta}^2)v - \tilde{B}\left[\left(\tilde{\mathrm{D}}^2 + \tilde{\beta}^2\right)\left(\frac{\tilde{\mathrm{D}}^2 v + \tilde{\beta}^2 v}{|\tilde{\mathrm{D}}U_b|}\right) - 4\tilde{\beta}^2\tilde{\mathrm{D}}\left(\frac{\tilde{\mathrm{D}}v}{|\tilde{\mathrm{D}}U_b|}\right)\right]. \tag{5.6}$$

The solutions to equations (5.5) and (5.6) can be divided into two eigenmode classes. The first one corresponds to the set of the eigenmodes of (5.6) with a particular solution of (5.5). The second class represents the set of eigenmodes of (5.5) with $v = 0$. Following the same method as for a streamwise perturbation, it can be shown that the solutions to (5.5) and (5.6) are imaginary, always damped and the Bingham term has a stabilizing effect. However, this effect is more significant for the eigenvalues of (5.6) than for those of (5.5). This result can be expected from a comparison of the highest derivative order in the Bingham term with that in the pure viscous dissipation term in (5.6) and (5.5). This is a consequence of the fact that the shear stress τ'_{xy} does not depend on $\tilde{B}$.

Finally, for fixed $\tilde{B}$, the increase of $\widetilde{Re}$ leads to a 'coalescence' of the eigenvalues near the real axis.

5.1.3. *Oblique perturbation:* $\alpha \neq 0$ *and* $\beta \neq 0$

In this situation, either the (u, v) or the (v, w) formulation can be used. The numerical results show that the shape of the eigenvalue spectrum is similar to that of Newtonian fluid, except that for Bingham fluid, there are two separated vertical branches, one of which can be associated to the Bingham–Squire modes described in § 5.1.1.

Finally, for the range of the parameters considered in the present study; we have not found any instability, thus, the PBPF is conjectured to be linearly stable. This is a consequence of the vanishing perturbation at the yield surface. The flow remains linearly stable even for $\tilde{B} \ll 1$, whereas for plane Newtonian Poiseuille flow (PNPF) and beyond $Re = 5772$ (Orszag 1971) a wall mode leaves the stable half-plane and the flow becomes unstable. The unmatched critical conditions at the limit $\tilde{B} = 0$ may be explained as follows (Metivier, Nouar & Brancher 2005). In the framework of the linear stability analysis, it is assumed implicitly that the perturbation is infinitesimally small with respect to all scales of the basic flow. In particular, one can write $\epsilon = o(\tilde{B})$. From (2.9), we have $y_0 = O(\tilde{B})$ as $\tilde{B} \to 0$, thus $\epsilon = o(y_0)$. Consequently the yield surfaces are linearly perturbed and the plug zone remains intact.

As explained at the beginning of this section, when the Bingham terms are cancelled artificially in the perturbation equations, we recover the linear stability problem of a PNCPF in which the upper plate is fixed and the lower plate is moving with a constant velocity U_c. According to Potter (1966), this type of flow is linearly stable

when the ratio of U_c to the maximum velocity of the Poiseuille velocity component $U_{p,max}$ is greater than 0.7. In the present study, $U_c/U_{p,max} = 4$.

The fact that the Bingham–Poiseuille flow is linearly stable means that the transitional Reynolds number moves to higher values when the magnitude of the disturbance decreases, pointing out the role of receptivity in determining the fate of the flow.

5.2. *Non-normality: pseudospectra and numerical range*

The eigenmodes characterize the behaviour of the disturbance as $t \to \infty$. Thus for PBPF, a perturbation introduced at $t = 0$ decays to zero for large times. The traditional approach of stability based on eigenvalues is not sufficient to describe the temporal behaviour of the disturbance at all times because of the non-normality of the linear stability operator. This mathematical property means that there is a potential for extraction of energy from the basic flow by a subspace of perturbations leading to transient growth, despite the absence of an exponential instability.

The non-normality of the linear stability operators $\mathscr{L} \equiv \mathscr{M}^{-1}_{vw(uv)}\mathscr{L}_{vw(uv)}$ (3.15) and (3.16) is characterized by using the ϵ-pseudospectrum and numerical range tools (see, for instance, Trefethen *et al.* 1993; Reddy, Schmid & Henningson 1993, and references therein). Let $\mathscr{C}$ be the discrete representation of $\mathscr{L}$. The ϵ-pseudospectrum of $\mathscr{C}$ is defined as the set of complex numbers z for which $\|(z\mathscr{I} - \mathscr{C})^{-1}\|_E \geqslant \epsilon^{-1}$, or equivalently, the set of complex numbers z which are eigenvalues of $\mathscr{C} + \Delta\mathscr{C}$ for some perturbation matrix $\Delta\mathscr{C}$ with $\|\Delta\mathscr{C}\|_E \leqslant \epsilon$. It is usually displayed graphically with contours of the norm of the resolvent $(z\mathscr{I} - \mathscr{C})^{-1}$ for various values of ϵ. The more non-normal the linear operator $\mathscr{L}$, the greater the potential of a disturbance operator $\Delta\mathscr{L}$ to affect the eigenvalues. The numerical range of $\mathscr{C}$ is the set of complex numbers $(\mathscr{C}\boldsymbol{q}, \boldsymbol{q})$, where $(.,.)$ is the inner product associated with the energy norm and $\boldsymbol{q}$ is a vector with a unit norm. We recall that an asymptotically stable non-normal operator supports transient energy growth if and only if its numerical range extends into the unstable half-plane. This section focuses on the effect of the Bingham terms on the variation of the ϵ-pseudospectra and numerical range in two- and three-dimensional situations.

5.2.1. *Streamwise perturbation*

For $\beta = 0$, the Bingham–Squire (BS) and Bingham–Orr-Sommerfeld (BOS) operators are decoupled. The BS operator is normal and its eigenvalues lie in the lower half-plane. Therefore, the numerical range also lies in the lower half-plane. The non-normality of the BOS operator is due to the term $U_b\,\tilde{\mathrm{D}}^2$ in the advection operator, where the coupling between the mean flow and the disturbance is concentrated. The operator associated with the Bingham term, i.e. $-4\tilde{\alpha}^2\tilde{B}\tilde{\mathrm{D}}(\tilde{\mathrm{D}}v/|\tilde{\mathrm{D}}U_b|)$ is self-adjoint. Figure 5 displays a spectral portrait of the BOS operator for $\tilde{\alpha} = 1$, $\widetilde{Re} = 3000$ and two values of $\tilde{B}$: 0.02 and 20. The iso-contours labelled p delineate the boundaries in the complex plane of the ϵ-pseudospectrum with $\epsilon = 10^{-p}$. The dotted line is the boundary of the numerical range. A comparison of figures 5(*a*) and 5(*b*) indicates that the effect of $\tilde{B}$ on the pseudospectra remains relatively small as expected according to the analysis in § 5.1.1.

As for BOS spectra, when $\tilde{\alpha} \neq 1$, the shape of the pseudospectra is not modified if they are represented in terms of $(\omega_r/\alpha, \omega_i/\alpha)$. In addition, according to (5.1), for fixed $\tilde{\alpha}\widetilde{Re}$ and $\tilde{\alpha}^2\tilde{B}$, when $\tilde{\alpha}$ increases, the extent of pseudospectra in the unstable half-plane is reduced because of the increase of the viscous dissipation.

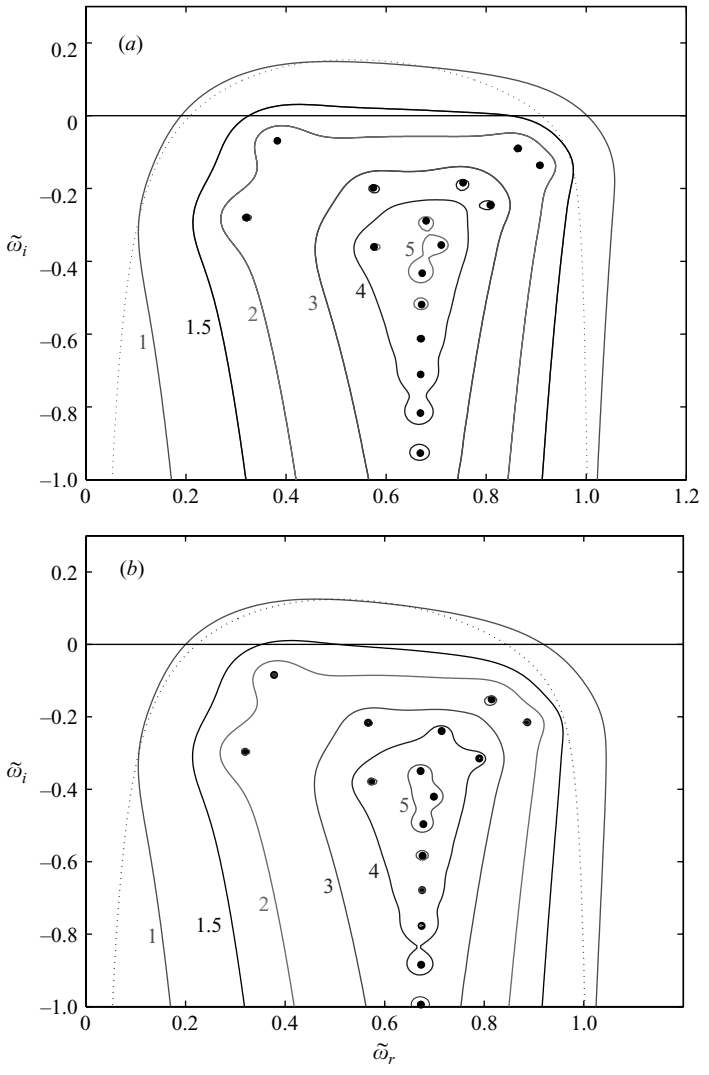

FIGURE 5. Pseudospectra of the Bingham–Orr–Sommerfeld operator. The computation was performed with $\tilde{\alpha} = 1$, $\widetilde{Re} = 3000$ and (*a*) $\tilde{B} = 0.02$, (*b*) $\tilde{B} = 20$ ($y_0 \approx 0.91$). Iso-contours labelled p delineate the boundaries in the complex plane of the ϵ-pseudospectrum with $\epsilon = 10^{-p}$. The dotted line is the boundary of the numerical range.

5.2.2. *Spanwise perturbation*

For $\alpha = 0$, the non-normality of the operator $\mathscr{M}_{uv}^{-1}\mathscr{L}_{uv}$ arises from the coupling operator, $-\widetilde{Re}\tilde{D}U_b$ in (5.5). Figure 6 shows the PBPF pseudospectra computed for $\tilde{\alpha} = 0$, $\tilde{\beta} = 3.4$, $\widetilde{Re} = 3000$ and two values of $\tilde{B}$: 0.02 and 20. The solid lines are the boundaries of the ϵ-pseudospectrum for $\epsilon = 10^{-1}, 10^{-1.5}, 10^{-2}, 10^{-3}, 10^{-4}$ and the dotted line is the boundary of the numerical range. An increase in $\tilde{B}$ significantly reduces the extent of the pseudospectrum in the upper half-plane. For instance, for $\tilde{B} = 0.02$, the operator requires a perturbation of $O(10^{-4})$ to protrude into the unstable region, while for $\tilde{B} = 20$, it requires a much more intense perturbation ($O(10^{-1.5})$). In

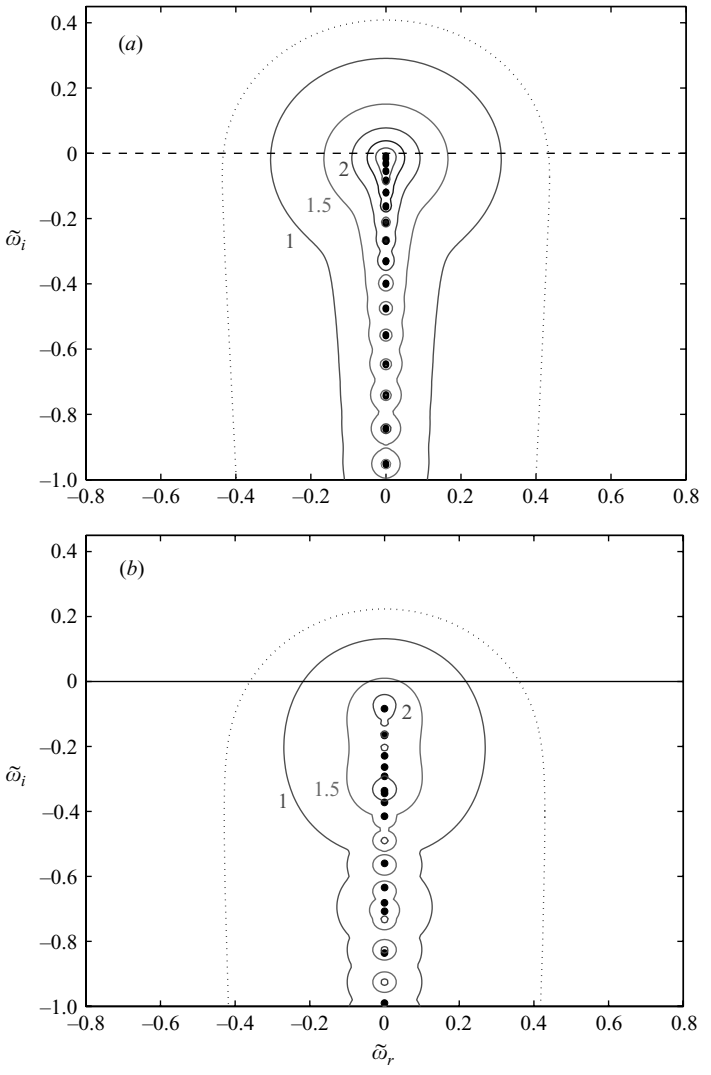

FIGURE 6. Pseudospectra for PBPF with $\tilde{\alpha} = 0$, $\tilde{\beta} = 3.4$, $\widetilde{Re} = 3000$ and (*a*) $\tilde{B} = 0.02$; (*b*) $\tilde{B} = 20$.

other words, the Bingham terms strongly reduce the degree of non-normality of the linear stability operator corresponding to a spanwise perturbation.

5.2.3. *Oblique perturbation*

For an oblique perturbation, $\tilde{\alpha} \neq 0$ and $\tilde{\beta} \neq 0$, the pseudospectra are qualitatively similar to those obtained for the two-dimensional operator with $\beta = 0$ and $\alpha \neq 0$. However, the effect of the Bingham number is more significant for the three-dimensional operator. This effect is clearly visible in figure 7 which illustrates the boundaries of the numerical range and the ϵ-pseudospectrum for $\epsilon = 10^{-2.2}$ and two values of $\tilde{B}$: 0.02 and 20. The other parameters are set to $\tilde{\alpha} = \tilde{\beta} = 1$ and $\widetilde{Re} = 3000$.

The non-normality of the stability operator means physically that some disturbances could experience a transient stage of energy amplification before conforming to the long-time modal prediction (exponential decay). The aim of the following section is

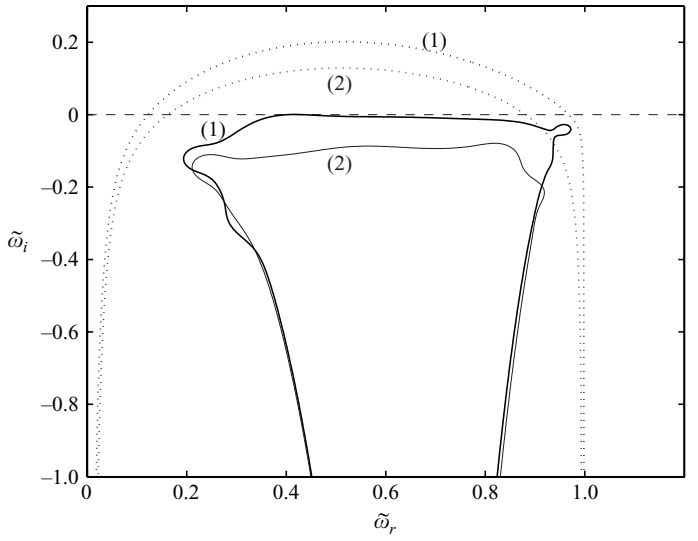

FIGURE 7. Boundaries of the numerical range (dotted line) and the ϵ-pseudospectrum (continuous line) with $\epsilon = 10^{-2.2}$ for $\widetilde{Re} = 3000$ and (1) $\tilde{B} = 0.02$; (2) $\tilde{B} = 20$.

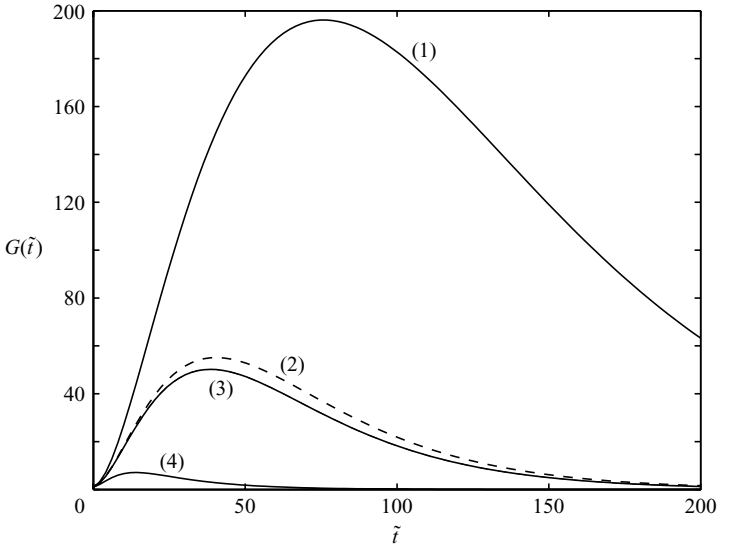

FIGURE 8. Energy amplification at $\tilde{\alpha} = 0$, $\tilde{\beta} = 2.04$ and $\widetilde{Re} = 10^3$: (1) PNPF, (2) PNCPF, (3) PBPF $\tilde{B} = 0.02$ and (4) PBPF $\tilde{B} = 2$.

to quantify the effect of $\tilde{B}$ on (i) the quantity of energy that can be extracted from the basic flow by a disturbance and (ii) the characteristics of the optimal disturbance.

5.3. *Transient energy growth and optimal perturbation*

Figure 8 shows plots of the amplification factor $G(\tilde{t})$ for PNPF, PNCPF and PBPF at $\widetilde{Re} = 1000$, $\tilde{\alpha} = 0$, $\tilde{\beta} = 2.04$ and two values of $\tilde{B}$: 0.02 and 2. It is observed that at very low Bingham number, the transient growth of disturbance of wavelength considered here is strongly reduced compared to PNPF. The origin of the discontinuous behaviour

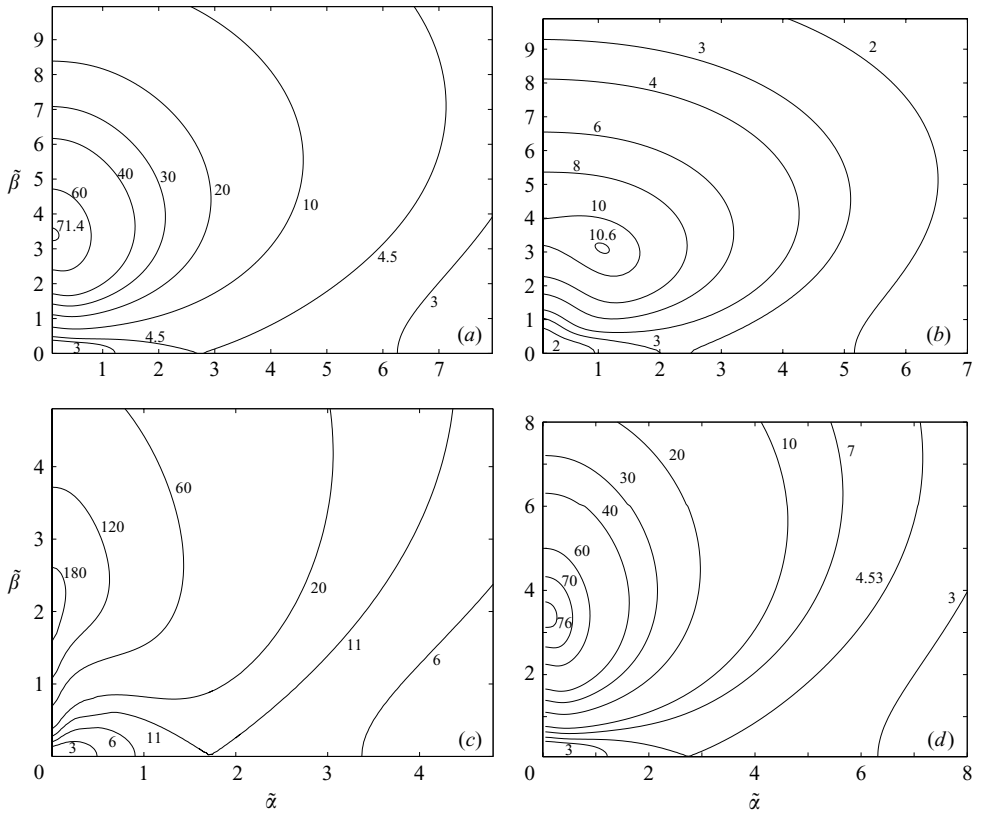

FIGURE 9. Contour plots of the maximum gain G^{max} in the $(\tilde{\alpha}, \tilde{\beta})$-plane at $\widetilde{Re} = 1000$ for PBPF with (*a*) $\tilde{B} = 0.02$; (*b*) $\tilde{B} = 2$ and for two reference flows, (*c*) PNPF and (*d*) PNCPF.

Flow	$\tilde{\alpha}^{opt}$	$\tilde{\beta}^{opt}$	G^{opt}	t^{opt}
Plane Newtonian Poiseuille flow	0	2.04	196	76
Plane Newtonian Couette–Poiseuille flow	0	3.40	77	33
Plane Bingham–Poiseuille flow ($\tilde{B} = 0.02$)	0	3.40	71.4	31.54
Plane Bingham–Poiseuille flow ($\tilde{B} = 2$)	1.07	3.11	10.62	8.96

TABLE 1. Characteristics of the optimal perturbation at $\widetilde{Re} = 1000$. Results for PNPF are in good agreement with Butler & Farrell (1992) and Reddy & Henningson (1993). For PNCPF, good agreement is found with Bergrström (2005).

of $G(\tilde{t})$ at the limit $B = 0$ was previously discussed. As $\tilde{B}$ increases, $G(\tilde{t})$ decreases because of the increase of the viscous dissipation. In addition, the growth period becomes shorter.

To obtain a more complete picture of the transient growth dependence on the wavenumbers, the maximum growth is calculated for a number of points in the $(\tilde{\alpha}, \tilde{\beta})$-plane. The contours of G^{max} are presented in the $(\tilde{\alpha}, \tilde{\beta})$-plane for $\widetilde{Re} = 1000$ and $\tilde{B} = 0.02$ (figure 9*a*), $\tilde{B} = 2$ (figure 9*b*) and two reference flows: PNPF (figure 9*c*) and PNCPF (figure 9*d*). The characteristics of the optimal perturbation are summarized in table 1. For PNCPF, the flow domain is delimited by the fixed wall at $\tilde{y} = 1$ and

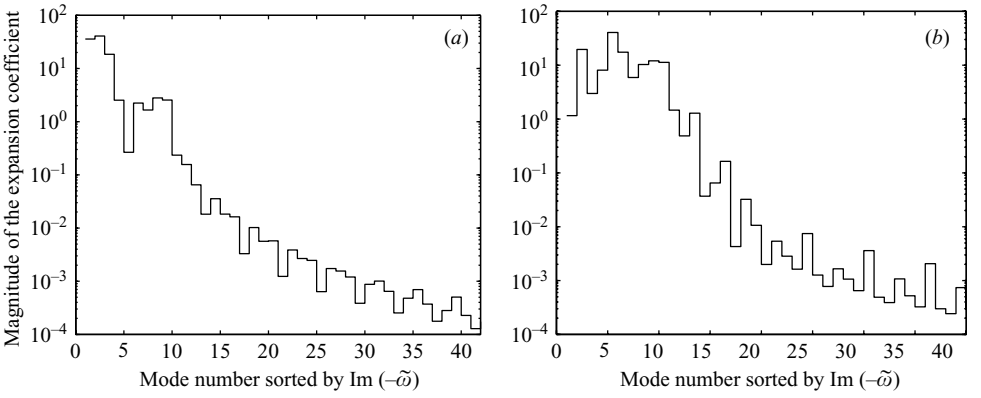

FIGURE 10. Projection of the optimal perturbation on the eigenmodes for $\widetilde{Re} = 1000$ and (*a*) $\tilde{B} = 0.02$; (*b*) $\tilde{B} = 2$.

the yield surface at $\tilde{y} = 0$ which plays the role of a moving plate. Therefore, in this situation, the characteristic scale length is implicitly the distance between the two walls at $\tilde{y} = 0$ and $\tilde{y} = 1$. Bergström (2005) used the half-distance between the two plates as a scale length and found that $\beta^{opt} = 1.7$.

The computations performed for different Re show that for sufficiently large Re we have: (i) $G^{opt} \approx 1.96 \times 10^{-4} \times Re^2$ and $t^{opt} \approx 0.076 \times Re$ in the case of PNPF, in agreement with Reddy & Henningson (1993) and (ii) $G^{opt} \approx 0.77 \times 10^{-4} \times Re^2$ and $t^{opt} \approx 0.033 \times Re$ in the case of PNCPF.

Consider now the PBPF, and figure 9(*a*). As expected, although $\tilde{B} \ll 1$, the values of G^{max} are significantly reduced everywhere in the $(\tilde{\alpha}, \tilde{\beta})$-plane compared to PNPF. The projection of the optimal perturbation on the eigenbasis, reported in figure 10(*a*), shows that the least damped modes are the main components of this optimal, as expected from the pseudospectrum.

Figures 11(*a*) and 11(*b*) display the velocity field $v\boldsymbol{e}_y + w\boldsymbol{e}_z$ of the optimal disturbance characterized by two counter-rotating vortices and the optimal streaks. Initially, the kinetic energy of the optimum perturbation is mainly in the v and w components. At $\tilde{t} = \tilde{t}^{opt}$, it is contained mainly in the u field. As explained by several authors (Butler & Farrell 1992; Asai & Nishioka 1989; Trefethen *et al.* 1993), the streamwise velocity grows linearly with time via a lift-up mechanism before being damped by the viscosity. The typical time scale for the evolution is the viscous one, thus the growth lasts a (non-dimensional) time $O(\widetilde{Re})$ and the streamwise velocity is amplified $\widetilde{Re}$ times, yielding an energy amplification scaling with $\widetilde{Re}^2$.

With increasing $\tilde{B}$, $G^{max}(\tilde{\alpha}, \tilde{\beta})$ decreases owing to the increase of the viscous dissipation, as shown in figure 9(*b*) for $\tilde{B} = 2$. The obliqueness of the optimal perturbation is a consequence of the nonlinear variation of the effective viscosity between the wall and the yield surface. Its projection on the eigenbasis represented in the figure 10(*b*) shows that it is constructed mainly with the eigenmodes corresponding to eigenvalues at or near the intersection of branches S, A and P (see figure 2). The development of the perturbation in the $(\tilde{x}, \tilde{y})$ and $(\tilde{y}, \tilde{z})$ cross-sections is shown in figures 12–14 at $\tilde{t} = 0, \tilde{t}^{opt}/2, \tilde{t}^{opt}$ and $3\tilde{t}^{opt}/2$. Initially, the contours of v are tilted in the direction opposite to the mean shear (figure 13*a*). As time evolves, the perturbation is tilted to a more upright orientation (figure 13*c*). At short time, not represented here, the vertical velocity is intensified. Thus, the perturbation gains energy by taking

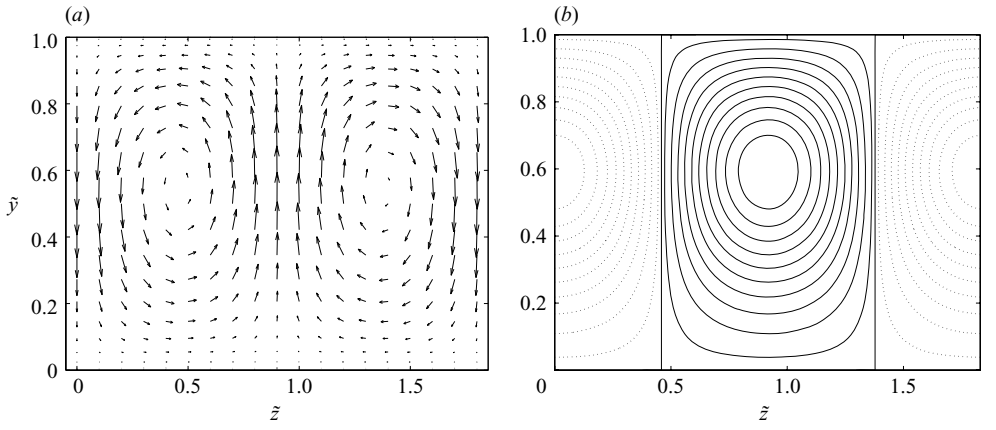

FIGURE 11. Optimal perturbation and optimal streaks at $\widetilde{Re} = 1000$ and $\tilde{B} = 0.02$. (*a*) Velocity vectors $v\boldsymbol{e}_y + w\boldsymbol{e}_z$ of the optimal perturbation at $t = 0$. (*b*) Streamwise velocity u contours at $t = t^{opt}$. The solid lines represent positive values and the dotted lines represent negative values. The same contour levels for the positive and negative values with respect to $|u|_{max}$ are plotted: [0.05, 0.15, ..., 0.95].

advantage of the two-dimensional Reynolds stress mechanism (Pedlosky 1987), in addition to the lift-up mechanism that causes the growth of u in figure 14.

A comprehensive study of the dependence of G^{opt}, $\tilde{t}^{opt}$, $\tilde{\alpha}^{opt}$, $\tilde{\beta}^{opt}$ and $\Theta = \tan^{-1}(\beta/\alpha)$ on the Bingham number was performed for different values of $\widetilde{Re}$: 1000, 3000, 6000 and 10^4, and the results are depicted in figure 15. Here, Θ is a measure of the obliqueness in terms of the angle of the wave vector $(\tilde{\alpha}, \tilde{\beta})$ with respect to the $\tilde{x}$-axis. For a spanwise perturbation, $\beta = 0$ and $\Theta = 0$, while for streamwise perturbation, $\alpha = 0$ and $\Theta = 90^\circ$.

As expected, with increasing $\tilde{B}$, G^{opt} decreases until reaching the limit $G^{opt} = 1$, corresponding to the no-energy-growth condition. For $\widetilde{Re} = 10^3$, this condition is reached at $\tilde{B} \approx 22$, as is shown by curve (1) in figure 15(*a*) where $G^{opt}/\widetilde{Re}^2 = 10^{-6}$ from $\tilde{B} \approx 22$. Also, for a given value of $\tilde{B}$, G^{opt} increases with increasing $\widetilde{Re}$. In the range of $\tilde{B}$ where the different curves coincide, G^{opt} varies as $\widetilde{Re}^2$, and the numerical results can be fitted by the relation $G^{opt} \approx 0.77 \times 10^{-4} \times \widetilde{Re}^2 \times \exp(-1.3\,\tilde{B}^{0.60})$. It is clear that the range of $\tilde{B}$ where $G^{opt} \propto \widetilde{Re}^2$ is wider for larger $\widetilde{Re}$. A similar analysis is made for the results presented in figure 15(*b*). In the range of $\tilde{B}$ where the different curves coincide, $\tilde{t}^{opt}$ varies proportionally to $\widetilde{Re}$ and the numerical results can be described by $\tilde{t}^{opt} \approx 0.033 \times \widetilde{Re} \times \exp(-1.04\tilde{B}^{0.45})$. It is not surprising to see $\tilde{t}^{opt}$ decreasing abruptly to zero when the condition of no energy growth is reached (curve 1 in figure 15*b*). The discontinuity in curve (2) corresponding to $\widetilde{Re} = 3000$ indicates that the optimal perturbation changes from oblique to spanwise (see also curve 2 in the figure 15*c*).

6. Condition for no energy growth

This section is devoted to the computation of conditions for which there is no growth of the perturbation kinetic energy. Assuming a unit mass density, the kinetic energy density of a three-dimensional perturbation confined to a single wavenumber

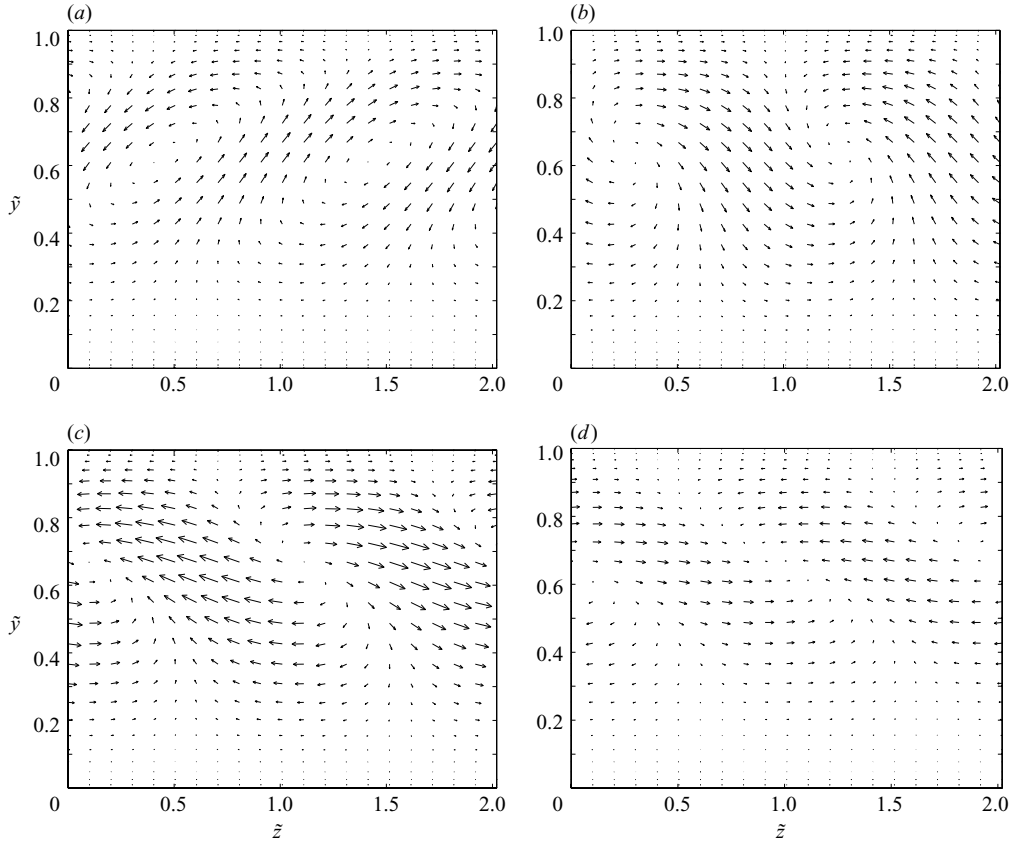

FIGURE 12. Velocity vectors $v\boldsymbol{e}_y + w\boldsymbol{e}_z$ at $x = 0$ for the optimal perturbation with $\widetilde{Re} = 1000$, $\tilde{B} = 2$, located at $\tilde{\alpha} = 1.07$, $\tilde{\beta} = 3.11$: (*a*) $\tilde{t} = 0$, $|v|_{max} = 1$, $G = 1$; (*b*) $\tilde{t} = 0.5\tilde{t}^{opt}$, $|v|_{max} = 0.915$, $G = 6.71$; (*c*) $\tilde{t} = \tilde{t}^{opt}$, $|v|_{max} = 0.509$, $G^{opt} = 10.619$; (*d*) $\tilde{t} = 1.5\tilde{t}^{opt}$, $|v|_{max} = 0.254$, $G = 7.466$. Here $t^{opt} = 8.98$ advective time units.

in the x- and z-directions is given by

$$E = \frac{1}{2}\frac{\alpha\beta}{4\pi^2}\frac{1}{1-y_0}\int_{y_0}^{1}\int_{0}^{2\pi/\alpha}\int_{0}^{2\pi/\beta}\left(u_r'^2 + v_r'^2 + w_r'^2\right)\mathrm{d}z\,\mathrm{d}x\,\mathrm{d}y, \tag{6.1}$$

where u_r' is the real part of $\{u(y,t)\exp[\mathrm{i}(\alpha x + \beta z)]\}$ and similarly for v_r' and w_r'. Using the continuity equation, E may be written in terms of $u(y,t)$ and $v(y,t)$ as

$$E = \frac{1}{4(1-y_0)}\int_{y_0}^{1}\left(\frac{k^2}{\beta^2}u^*u + v^*v + \frac{1}{\beta^2}\mathrm{D}v^*\mathrm{D}v + \frac{\mathrm{i}\alpha}{\beta^2}(\mathrm{D}v^*u - u^*\mathrm{D}v)\right). \tag{6.2}$$

Modulo the factor $(4(1-y_0))^{-1}$, the E expression is the norm energy defined by (3.17) and (3.18). Therefore, there is no energy growth if $(\mathrm{d}/\mathrm{d}t)\|\boldsymbol{q}\|_E^2 < 0$, with $\boldsymbol{q} = (u, v)^T$:

$$\frac{\mathrm{d}}{\mathrm{d}t}\|\boldsymbol{q}\|_E^2 = \left(\boldsymbol{q}, \frac{\mathrm{d}\boldsymbol{q}}{\mathrm{d}t}\right)_E + \left(\frac{\mathrm{d}\boldsymbol{q}}{\mathrm{d}t}, \boldsymbol{q}\right)_E = (\boldsymbol{q}, -\mathrm{i}\mathscr{A}_{uv}\boldsymbol{q})_E + (-\mathrm{i}\mathscr{A}_{uv}\boldsymbol{q}, \boldsymbol{q})_E = 2\mathrm{Im}(\mathscr{A}_{uv}\boldsymbol{q}, \boldsymbol{q})_E,$$

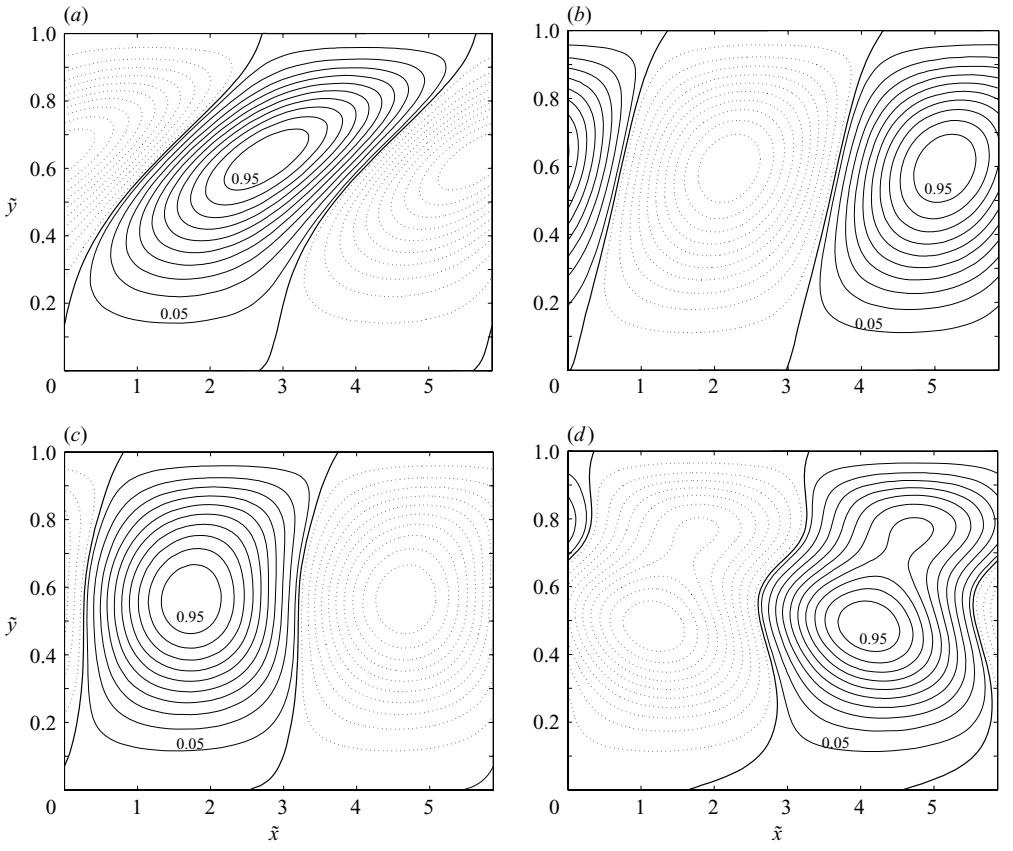

FIGURE 13. Normal velocity v contours at $z=0$ for the optimal perturbation with $\widetilde{Re}=1000$, $\tilde{B}=2$, located at $\tilde{\alpha}=1.07, \tilde{\beta}=3.11$: (*a*) $\tilde{t}=0, |v|_{max}=1, G=1$; (*b*) $\tilde{t}=0.5\tilde{t}^{opt}, |v|_{max}=0.915, G=6.71$; (*c*) $\tilde{t}=\tilde{t}^{opt}, |v|_{max}=0.509, G^{opt}=10.619$; (*d*) $\tilde{t}=1.5\tilde{t}^{opt}, |v|_{max}=0.254, G=7.466$.

where $\mathscr{A}_{uv} \equiv \mathscr{M}_{uv}^{-1}\mathscr{L}_{uv}$ from (3.16). After some manipulations, it can be shown that

$$\mathrm{Im}(\mathscr{A}_{uv}\boldsymbol{q}, \boldsymbol{q})_E = \mathscr{I}(\boldsymbol{u}) - \frac{1}{Re}[\mathscr{V}(\boldsymbol{u}) + \mathscr{B}(\boldsymbol{u})] \tag{6.3}$$

where $\mathscr{I}(\boldsymbol{u})$, $\mathscr{V}(u)/Re$ and $\mathscr{B}(\boldsymbol{u})/Re$ denote the inertial, viscous and Bingham terms, defined by

$$\mathscr{I}(\mathbf{u}) = -\langle (u_r v_r + u_i v_i)\mathrm{D}U \rangle \tag{6.4}$$

$$\mathscr{V}(\mathbf{u}) = \langle |\mathrm{D}\mathbf{u}|^2 + (\alpha^2+\beta^2)|\mathbf{u}|^2 \rangle \tag{6.5}$$

$$\mathscr{B}(\boldsymbol{u}) = B\left\langle \frac{3|\mathrm{D}v|^2 + k^2|u|^2}{|\mathrm{D}U|} \right\rangle + B\left\langle \frac{k^2|\alpha u - \mathrm{i}\mathrm{D}v|^2 + |\alpha \mathrm{D}u - \mathrm{i}(\mathrm{D}^2 v + \beta v)|^2}{\beta^2 |\mathrm{D}U|} \right\rangle, \tag{6.6}$$

where

$$|u|^2 = u_r^2 + u_i^2,\ |\boldsymbol{u}|^2 = |u|^2 + |v|^2 + |-\frac{\alpha}{\beta}u + \frac{\mathrm{i}}{\beta}\mathrm{D}v|^2, \text{ and } \langle\cdot\rangle = \int_{y_0}^{1} (\cdot)\,\mathrm{d}y.$$

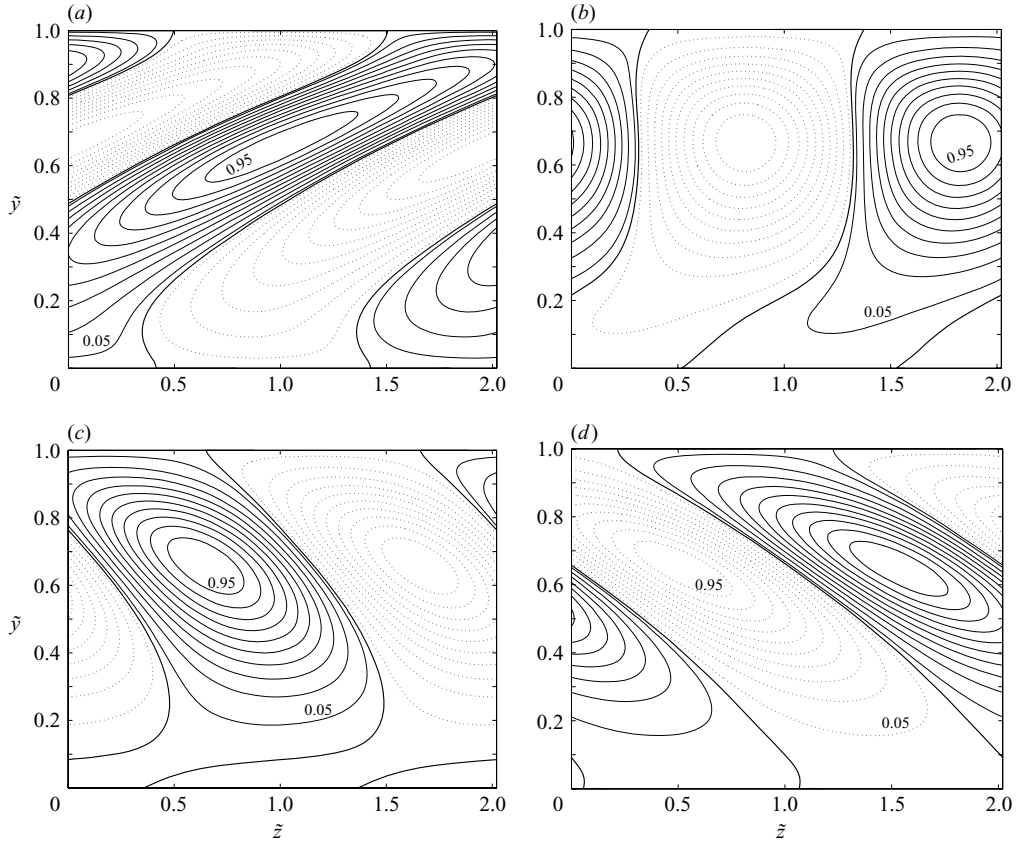

FIGURE 14. Streamwise velocity contours at $x = 0$ for the optimal perturbation with $\widetilde{Re} = 1000$, $\tilde{B} = 2$, located at $\tilde{\alpha} = 1.07$, $\tilde{\beta} = 3.11$: (*a*) $\tilde{t} = 0, G = 1, |u|_{max} = 0.943$, (*b*) $\tilde{t} = 0.5\tilde{t}^{opt}, G = 6.71, |u|_{max} = 5.022$, (*c*) $\tilde{t} = \tilde{t}^{opt}, G^{opt} = 10.619, |u|_{max} = 6.714$ and (*d*) $\tilde{t} = 0.5\tilde{t}^{opt}, G = 7.466, |u|_{max} = 5.622$. Values of u are normalized by the maximum value of v at time $\tilde{t} = 0$.

There is no energy growth if the right-hand side of (6.3) is negative. Define Re_1 as the largest value of Re such that this condition is satisfied:

$$\frac{1}{Re_1} = \sup_{\boldsymbol{u}} \frac{\mathscr{I}(\boldsymbol{u})}{\mathscr{V}(\boldsymbol{u}) + \mathscr{B}(\boldsymbol{u})}, \tag{6.7}$$

where $\boldsymbol{u}$ is an admissible perturbation satisfying the continuity equation and the boundary conditions. This optimization problem can be solved using variational calculus. The corresponding Euler equations are

$$\mathscr{F}^2 v + B\mathscr{H}(u, v) = -\frac{\lambda}{2}[k^2 u \mathrm{D}U_b + \mathrm{i}\alpha \mathrm{D}(v\mathrm{D}U_b)], \tag{6.8}$$

$$k^2 \mathscr{F} u - \mathrm{i}\alpha \mathrm{D}(\mathscr{F} v) - B\left[\frac{k^4 u - \mathrm{i}\alpha^3 \mathrm{D}v}{|\mathrm{D}U_b|} + \alpha \mathrm{D}\left(\frac{\mathrm{D}(\mathrm{i}\mathrm{D}v - \alpha u)}{|\mathrm{D}U_b|}\right)\right] = \lambda \frac{\beta^2}{2} \mathrm{D}U_b v, \tag{6.9}$$

where

$$\mathscr{H}(u, v) = -4k^2 \mathrm{D}\left(\frac{\mathrm{D}v}{|\mathrm{D}U_b|}\right) - \mathrm{i}(\mathrm{D}^2 + k^2)\left[\frac{\mathrm{D}(-\alpha u + \mathrm{i}\mathrm{D}v) + \mathrm{i}\beta^2 v}{|\mathrm{D}U_b|}\right].$$

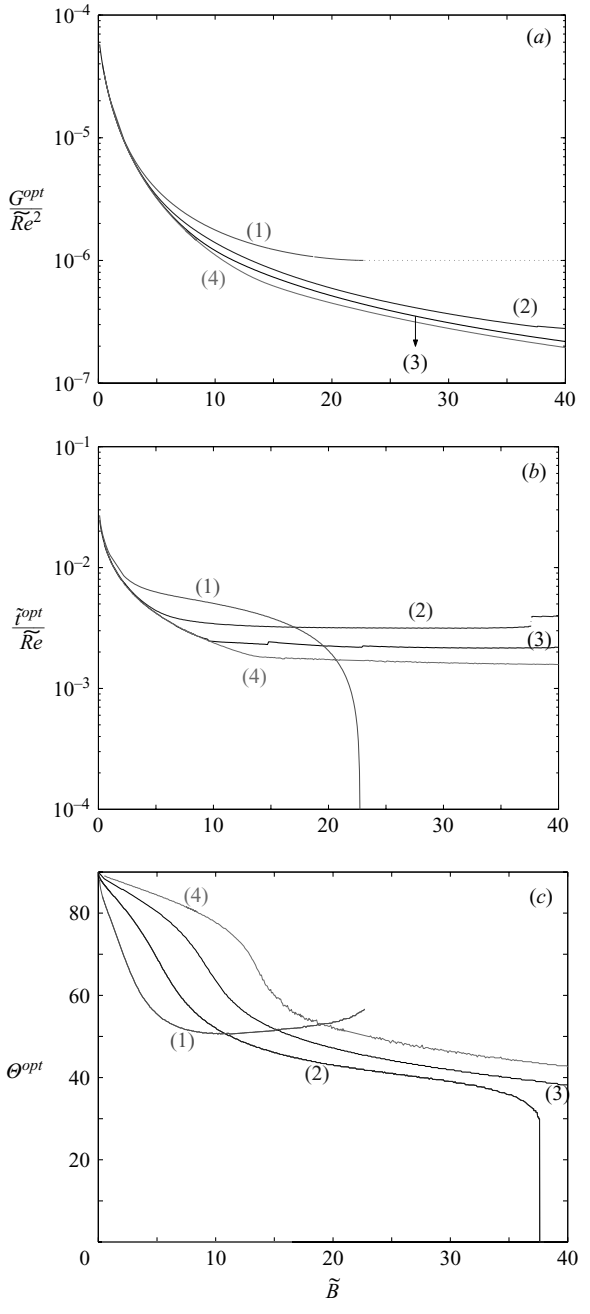

FIGURE 15. Variation of: (*a*) $G^{opt}/\widetilde{Re}^2$, (*b*) $t^{opt}/\widetilde{Re}$ and (*c*) Θ^{opt} as a function of $\tilde{B}$ for four different values of $\widetilde{Re}$: (1) $\widetilde{Re} = 1000$, (2) $\widetilde{Re} = 3000$, (3) $\widetilde{Re} = 6000$ and (4) $\widetilde{Re} = 10^4$.

The boundary conditions are

$$y = y_0; \quad u = v = \mathrm{D}v = 0, \tag{6.10}$$

$$y = 1; \quad u = v = \mathrm{D}v = 0. \tag{6.11}$$

Flow	$\tilde{\alpha}$	$\tilde{\beta}$	$\widetilde{Re}_E$
Plane Newtonian Poiseuille flow	0	2.04	49.60
Plane Newtonian Couette–Poiseuille flow	0	3.178	79.72
Plane Bingham–Poiseuille flow $(\tilde{B}=0.02)$	0	3.21	82.41
Plane Bingham–Poiseuille flow $(\tilde{B}=8)$	0.768	2.012	493.15
Plane Bingham–Poiseuille flow $(\tilde{B}=38)$	0.683	0	1342.5

TABLE 2. Critical conditions for no energy growth.

The function $Re_1(\alpha, \beta, B)$ is the smallest positive eigenvalue λ of (6.8)–(6.11).

If $\beta=0$, the (v, w) formulation is adopted and $Re_1(\alpha, 0, B)$ is the smallest positive eigenvalue of

$$(\mathrm{D}^2-\alpha^2)^2 v - 4\alpha^2 B \mathrm{D}\left(\frac{\mathrm{D}v}{|\mathrm{D}U|}\right) = -\mathrm{i}\alpha\frac{\lambda}{2}[2\mathrm{D}v\mathrm{D}U + v\mathrm{D}^2U], \tag{6.12}$$

with

$$y = y_0; \quad v = \mathrm{D}v = 0, \tag{6.13}$$

$$y = 1; \quad v = \mathrm{D}v = 0. \tag{6.14}$$

The numerical resolution of the eigenvalue problems (6.8)–(6.11) and (6.12)–(6.14) is based on the procedure described previously for mapping $[y_0, 1]$ onto $[0, 1]$ and re-scaling the flow properties and the controlling parameters.

Figure 16(a–c) illustrates the contours of $\widetilde{Re_1}$ in the $(\tilde{\alpha}, \tilde{\beta})$-plane, which separate regions of initial energy density growth from regions of initial energy decay, for $\tilde{B}=0.02$, 8 and 38, respectively. The contour $\widetilde{Re}_{1p}$ at which the energy growth region is delimited by inner and outer boundaries is indicated with a thick line. For $\tilde{B}=0.02$ and 8, $\widetilde{Re}_{1p}$ is reached at $\beta=0$, while for $\tilde{B}=38$, it is reached at $\alpha=0$.

Furthermore, it can be shown that $\widetilde{Re}_1(\tilde{\alpha}, \tilde{\beta}) \to \infty$ as $\tilde{\alpha}, \tilde{\beta} \to 0$ or $\tilde{\alpha}, \tilde{\beta} \to \infty$. Using Cauchy–Schwarz, Poincaré and triangle inequalities, Frigaard & Nouar (2003) showed that there is no energy growth if

$$Re \leqslant Re_1 = \frac{2y_0}{B\delta}\left[\frac{\pi^2+\delta^2(1-y_0)(1+2k_2y_0-y_0)}{(1-y_0)^4}\right], \tag{6.15}$$

with $\alpha=\delta\cos\phi$, $\beta=\delta\sin\phi : \phi \in [0, \pi/2]$. From equation (6.15), it is clear that $Re_1 \to \infty$ as $\delta \to 0$ or $\delta \to \infty$.

The maximum Reynolds number $\widetilde{Re}_E = \min_{\tilde{\alpha},\tilde{\beta}} \widetilde{Re}_1(\tilde{\alpha}, \tilde{\beta})$ that ensures no energy growth is given with the associated wavenumbers in table 2 for different $\tilde{B}$. For comparison, the critical values, $\tilde{Re}_E, \alpha_E$ and β_E, for PNPF and PNCPF are also given. For PNPF, the results are in very good agreement with those reported by Busse (1969) and Joseph & Carmi (1969). For $\tilde{B}=0.02$, we have $\tilde{Re}_E=82.41$, which is close to that obtained for PNCPF, that is $\tilde{Re}_E=79.82$. The numerical results show that $\tilde{Re}_E \to 79.82$ as $\tilde{B} \to 0$, while for PNPPF we have $\widetilde{Re}_E=49.6$. The origin of this discontinuous behaviour at $\tilde{B}=0$ has already been discussed in § 5.1.

The evolution of $\widetilde{Re}_E$ with $\tilde{B}$ is shown by curve 1 in figure 17. The conditional stability boundary (curve 2) derived in Nouar & Frigaard (2001) is also displayed, where purely viscous dissipation was used for deriving the stability bounds. The effect

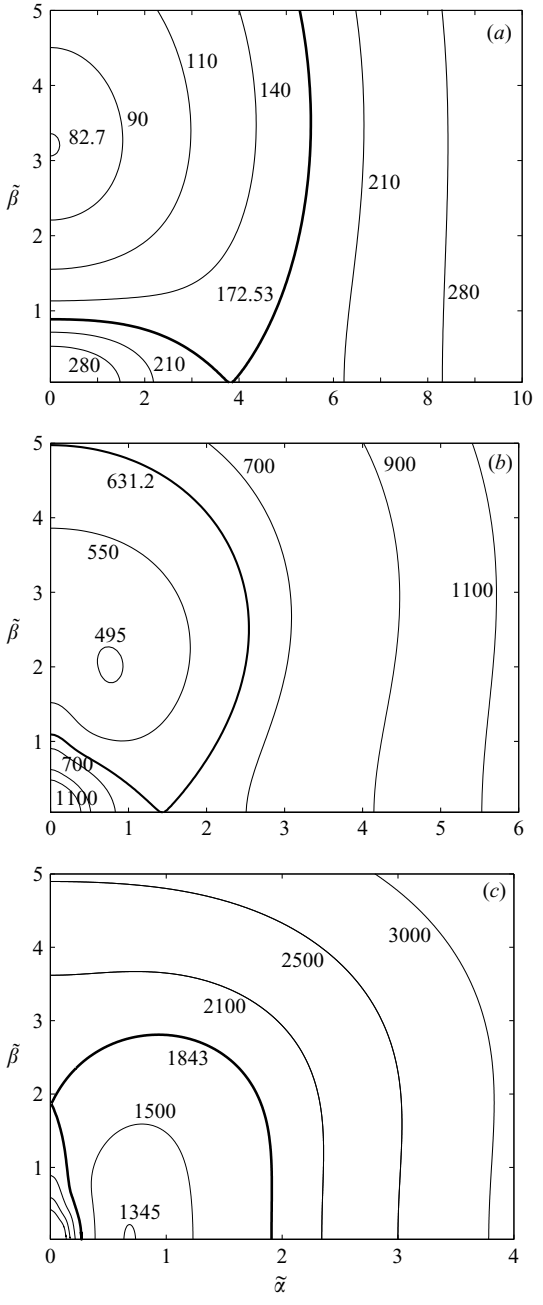

FIGURE 16. Contours of $\widetilde{Re}_1\left(\tilde{\alpha}, \tilde{\beta}\right)$ for (*a*) $\tilde{B} = 0.02$, (*b*) $\tilde{B} = 8$ and (*c*) $\tilde{B} = 38$.

of the yield stress was to reduce the width of the yielded region. For large $\tilde{B}$ ($\tilde{B} \geqslant 30$), $\widetilde{Re}_E$ varies as $\tilde{B}^{1/2}$. The numerical results may be fitted as: $\widetilde{Re}_E \approx 217\tilde{B}^{1/2}$.

The critical wavenumbers $\tilde{\alpha}_E$ and $\tilde{\beta}_E$ are represented as functions of $\tilde{B}$ in figure 18 and are also summarized in table 2. For $\tilde{B} < 4$, the most dangerous perturbation is in the spanwise direction ($\alpha = 0$), with a slow decrease of $\tilde{\beta}_E$ from 3.18 to 2.77.

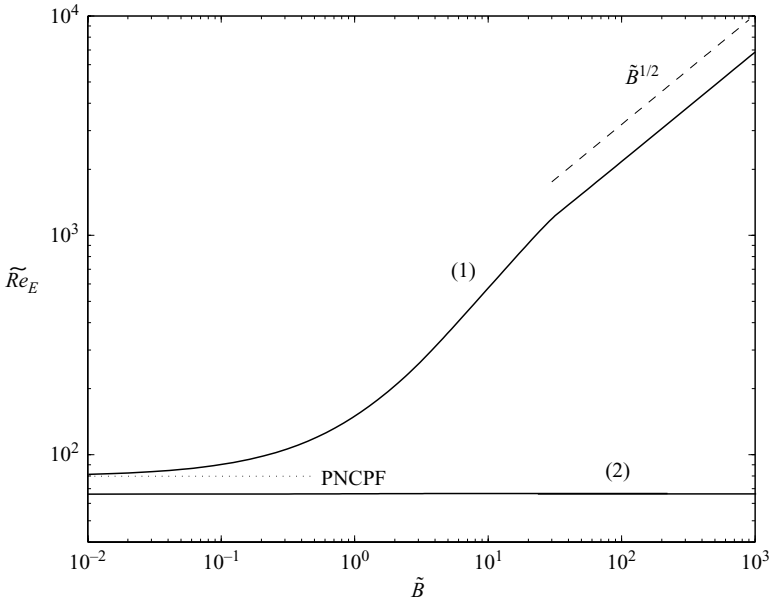

FIGURE 17. Critical Reynolds number versus $\tilde{B}$: (1) linear analysis; (2) conditional stability bound (Nouar & Frigaard 2001). The dashed line shows a $\tilde{B}^{1/2}$ variation for large $\tilde{B}$ and the dotted line is the limit of Re_E as $\tilde{B} \to 0$, i.e. PNCPF.

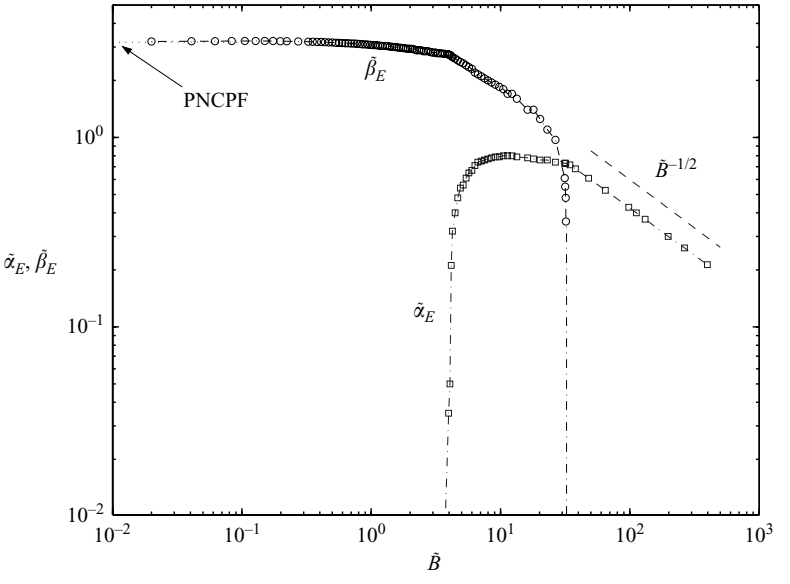

FIGURE 18. Critical streamwise $\tilde{\alpha_E}$ (curve with squares) and spanwise $\tilde{\beta_E}$ (curve with circles) wavenumbers versus $\tilde{B}$. The dashed line shows a $\tilde{B}^{-1/2}$ variation. The arrow indicates that as $\tilde{B} \to 0$, $\tilde{\beta}_E$ tends to the value corresponding to PNCPF.

For $\tilde{B} > 32$, the most dangerous perturbation is in the streamwise direction ($\beta = 0$, see figure 16*c*). Furthermore, for large $\tilde{B}$, the numerical results show that $\tilde{\alpha}$ evolves proportionally to $\tilde{B}^{-0.5}$. This result confirms and improves the result obtained by Frigaard & Nouar (2003), who have shown that $\sqrt{\tilde{\alpha}^2 + \tilde{\beta}^2}$ evolves proportionally

to $\tilde{B}^{-0.5}$. In terms of quantities without a tilde we have $\alpha_E \sim B^{1/4}$; thus the short-wavelength perturbations are the most dangerous. Finally, for $4 < \tilde{B} < 32$ the most dangerous perturbation is oblique. The viscous dissipation is much more sensitive to the Bingham number for spanwise than for streamwise disturbances. The variation of the critical wavenumbers with B is probably a consequence of the anisotropy of the shear-stress tensor perturbation due to the shear thinning character of the effective viscosity

7. Conclusion and discussion

In this paper, the linear stability analysis and the receptivity of the plane Poiseuille flow of a Bingham fluid have been thoroughly investigated using modal and non-modal approaches.

The modal approach led to the following results: First, for a streamwise perturbation, the effect of B is reduced essentially to the variation of the plug zone width and of the inertial terms, because τ'_{xy} is independent of B. For spanwise and oblique perturbations, the dissipation role of B is significant. Second, the plane Bingham–Poiseuille flow is linearly stable. This is a consequence of the vanishing perturbation at the yield surface. This condition arises from the Bingham model which imposes that the plug zone moves as a rigid body and, in our case, can have only a linear motion. Also, it can be conjectured that the Poiseuille flow of Bingham fluid in circular and annular pipes is linearly stable. This result can be extended to the Herschel–Bulkley, Casson or similar models, which assume that, below the yield stress, $\dot{\gamma} = 0$.

The non-normality of the linear stability operator was characterized using the ϵ-pseudospectrum and the numerical range tools. It was shown that the Bingham terms reduce the degree of non-normality. However, this effect is much weaker for a streamwise perturbation than for a spanwise or oblique perturbation. The most relevant results deduced from the non-modal approach are: First, the vanishing of the disturbance at the yield surface and the increase of the viscous dissipation induced by the Bingham terms reduce the energy transient growth compared to PNPF for any $(\tilde{\alpha}, \tilde{\beta})$. Second, for $\tilde{B} \ll 1$, the optimal perturbation is almost streamwise vortices with $\tilde{\alpha} \approx 0$ and $\tilde{\beta} \approx 3.4$. The algebraic growth of the kinetic energy is provided by the lift-up mechanism and the $\widetilde{Re}^2$ scalings for G_{opt} and $\widetilde{Re}$ for $\tilde{t}_{opt}$ were recovered. In contrast, for $\tilde{B} = O(1)$ or $\tilde{B} > 1$, the optimal perturbation is oblique. It gains energy by a combination of Orr and lift-up mechanisms. This obliqueness is a consequence of the anisotropy of the perturbation shear stress tensor induced by the dependence of the effective viscosity on the shear rate.

Finally, the maximum Reynolds number $\widetilde{Re}_E$ below which there is no energy growth was determined for a large range of $\tilde{B}$. The numerical results showed that for $\tilde{B} \ll 1$, $\widetilde{Re}_E \approx 79.8$ and the most dangerous perturbation is streamwise with $\tilde{\beta} = 3.21$. For large $\tilde{B}$ ($\tilde{B} \geqslant 30$), $\widetilde{Re}_E$ may be approximated as $\widetilde{Re}_E \approx 217\,\tilde{B}^{1/2}$ and the most dangerous perturbation is spanwise with $\tilde{\alpha}$ evolving proportionaly to $\tilde{B}^{-0.5}$. The variation of the critical wavenumbers with B is due to the shear-thinning character of the fluid.

The analysis presented shows the limits of the linear theory. In particular an investigation of the breakup of the plug zone, physically important especially for low Bingham numbers, cannot be done without accounting of nonlinear effects.

REFERENCES

Asai, M. & Nishioka, M. 1989 Origin of the peak-valley wave structure leading to wall turbulence. *J. Fluid Mech.* **208**, 1–23.

Bergström, L. B. 2005 Nonmodal growth of three-dimensional disturbances on plane Couette–Poiseuille flows. *Phys. Fluids* **17**, 014105, 1–10.

Beris, A. N., Tsamopoulos, J. A., Armstrong, R. C. & Brown, R. A. 1985 Creeping motion of a sphere through a Bingham plastic. *J. Fluid Mech.* **158**, 219–244.

Bird, R. B., Dai, G. C. & Yarusso, B. J. 1983 The rheology and flow of viscoplastic materials. *Rev. Chem. Engng* **1**, 1–70.

Busse, F. H. 1969 Bounds on the transport of mass and momentum by turbulent flow between parallel plates. *J. Angew. Math. Phys.* **20**, 1–14.

Butler, K. M. & Farrell, B. F. 1992 Three-dimensional optimal perturbations in viscous shear flow. *Phys. Fluids* A **4**, 1637–1650.

Coussot, P. 1999 Saffman-Taylor instability in yield-stress fluids. *J. Fluid Mech.* **380**, 363–376.

Farrell, B. F. 1988 Optimal excitation of perturbations in viscous shear flow. *Phys. Fluids* **31**, 2093–2102.

Frigaard, I. A., Howison, S. D. & Sobey, I. J. 1994 On the stability of Poiseuille flow of a Bingham fluid. *J. Fluid Mech.* **263**, 133–150.

Frigaard, I. A. & Nouar, C. 2003 On three-dimensional linear stability of Poiseuille flow of Bingham fluids. *Phys. Fluids* **15**, 2843–2851.

Georgievskii, D. V. 1993 Stability of two and three dimensional viscoplastic flows, and generalized Squire theorem. *Izv. AN SSSR. Mekhanica Tverdogo Tela.* **28**, 117–123.

Gustavsson, L. H. 1991 Energy growth of three-dimensional disturbances in plane Poiseuille flow. *J. Fluid Mech.* **224**, 241–260.

Hanks, R. W. 1963 The laminar-turbulent transition for fluids with a yield stress. *AIChE J.* **9**, 306–309.

Hanks, R. W. & Pratt, D. R. 1967 On the flow of Bingham plastic slurries in pipes and between parallel plates. *SPEJ* **7**, 342–346.

Hedström, B. O. A. 1952 Flow of plastic materials in pipes. *Ind. Engng Chem.* **44**, 651–656.

Henningson, D. S., Lundbladh, A. & Johansson, A. V. 1993 A mechanism for bypass transition from localized disturbances in wall-bounded shear flows. *J. Fluid Mech.* **250**, 169–207.

Joseph, D. D. & Carmi, S. 1969 Stability of Poiseuille flow in pipes, annuli and channels. *Q. Appl. Maths* **26**, 575–599.

Khorrami, M. R., Malik, M. R. & Ash, R. L. 1989 Application of spectral collocation techniques to the stability of swirling flows. *J. Comput. Phys.* **81**, 206–229.

Klingmann, B. G. B. 1992 On transition due to three-dimensional disturbances in plane Poiseuille flow. *J. Fluid Mech.* **240**, 167–195.

Mack, L. M. 1976 A numerical study of the temporal eigenvalue spectrum of the Blasius boundary layer. *J. Fluid Mech.* **73**, 497–520.

Métivier, C., Nouar, C. & Brancher, J. P. 2005 Linear stability involving the Bingham model when the yield stress approaches zero. *Phys. Fluids* **17**, 104106, 1–7.

Metzner, A. B. & Reed, J. C. 1955 Flow of Non-Newtonian Fluids – Correlation of laminar, transition and turbulent flow regions. *AIChE J.* **1**, 434–440.

Mishra, P. & Tripathi, G. 1971 Transition from laminar to turbulent flow of purely viscous non-Newtonian fluids in tubes. *Chem. Engng Sci.* **26**, 915–921.

Nouar, C. & Frigaard, I. 2001 Nonlinear stability of Poiseuille flow of a Bingham fluid : theoretical results and comparison with phenomenological criteria. *J. Non-Newtonian Fluid Mech.* **100**, 127–149.

Oldroyd, J. G. 1947*a* A rational formulation of the equations of plastic flow for a Bingham solid. *Proc. Camb. Phil. Soc.* **43**, 100–105.

Oldroyd, J. G. 1947*b* Two dimensional plastic flow of a Bingham solid. A plastic boundary-layer theory for slow motion. *Proc. Camb. Phil. Soc.* **43**, 383–395.

Orszag, S. A. 1971 Accurate solution of the Orr-Sommerfeld stability equation. *J. Fluid Mech.* **50**, 689–703.

Pedlosky, J. 1987 *Geophysical Fluid Dynamics*, section 7.3. Springer.

Potter, M. C. 1966 Stability of plane Couette–Poiseuille flow. *J. Fluid Mech.* **24**, 609–619.

Reddy, S. C. & Henningson, D. S. 1993 Energy growth in viscous channel flows. *J. Fluid Mech.* **252**, 209–238.

Reddy, S. C., Schmid, P. J. & Henningson, D. S. 1993 Pseudospectra of the Orr-Sommerfeld operator. *SIAM J. Appl. Maths* **53**, 15–47.

Ryan, N. W. & Johnson, M. M. 1959 Transition from laminar to turbulent flow in pipes *AIChE J.* **5**, 433–435.

Schmid, P. J. & Henningson, D. S. 1994 Optimal energy density growth in Hagen-Poiseuille flow. *J. Fluid Mech.* **277**, 197–225.

Schmid, P. J. & Henningson, D. S. 2000 *Stability and Transition in Shear Flows*. Springer.

Slatter, P. T. 1999 The laminar turbulent transition prediction for non-Newtonian slurries. *Proc. Intl Conf. on Problems in Fluid Mechanics and Hydrology, Prague* (ed. P. Vlasák), Vol. 1, pp. 247–256. Institute of Hydrodynamics AS CR, Czech Republic.

Synge, J. L. 1938 Hydrodynamic stability. *Semi-Centenn. Publ. Am. Math. Soc.* **2**, 227–269.

Trefethen, L. N., Trefethen, A. E., Reddy, S. C. & Driscoll, T. A. 1993 Hydrodynamic stability without eigenvalues. *Science* **261**, 578–584.